University of Iowa

Iowa Research Online

Theses and Dissertations

Summer 2017

Flow regimes and instabilities of propeller crashback

Matthew Pontarelli
University of Iowa

Flow Regimes and Instabilities of Propeller Crashback

by

Matthew Pontarelli

A thesis submitted in partial fulfillment
of the requirements for the Master of Science
degree in Mechanical Engineering in the
Graduate College of
The University of Iowa

August 2017

Thesis Supervisors: Professor Pablo M. Carrica
Dr. Juan Ezequiel Martin

Graduate College
The University of Iowa
Iowa City, Iowa

CERTIFICATE OF APPROVAL

_____

MASTER'S THESIS

_____

This is to certify that the Master's thesis of

Matthew Pontarelli

has been approved by the Examining Committee for
the thesis requirement for the Master of Science degree
in Mechanical Engineering at the August 2017 graduation.

Thesis Committee: _____

Pablo M. Carrica, Thesis Supervisor

_____

Juan Ezequiel Martin, Thesis Supervisor

_____

James H. Buchholz

To my friend Jeff and his family, my parents and my sisters.

ACKNOWLEDGEMENTS

Thank you to my degree advisor Professor Carrica for picking an intriguing topic of fluid mechanics. I would also like to thank Professor Carrica and Dr. Juan Ezequiel Martin for their patience, guidance and contribution to this analysis. I would like to recognize Dr. Ki-Han Kim from the Office of Naval Research (program manager) for providing funding for my Master's program.

Thank you to my fellow students at IIHR for their academic support. I would like to recognize the faculty of the fluid/thermal graduate program that expanded my knowledge of the subject through their passionate teaching. Thank you to my close friends and loved ones that gave continuous support throughout my Master's program.

ABSTRACT

Crashback operation of a propeller is a common emergency slowing maneuver for ships and submarines. The reversing of the propeller while the vessel is moving forward results in large loads on the propeller blades and highly detached flow, which presents both practical concerns and fundamental fluid physics inquiries. This thesis contains a comprehensive numerical analysis of two propellers in crashback operation. Available numerical and experimental data for David Taylor Model Basin (DTMB) 4381 propeller are used for validation of the computational fluid dynamics solver used, REX. A second propeller, Maritime Research Institute Netherlands (MARIN) 7371R is used to classify the common crashback flow behavior into regimes. Four regimes were identified, each existing for a range of operating conditions. The most prominent and deciding feature of the flow regimes is the presence of a ring vortex, resulting from the opposing action of the free-stream flow and the propeller induced flow. The position, shape and strength changes between regimes, dominating the dynamics of the flow by altering the induced flow into the propeller disk. Flow conditions resulting from regime transitions are described. Changes in the ring vortex structure lead to two stable flow conditions of interest. One condition produces a reduction of thrust despite the increase in flow speed into the propeller and negligible side-forces. The other condition creates large side-forces capable of rotating a vessel, resulting from an asymmetry forming in the ring vortex. Additionally, massive flow separation occurs at high free-stream speeds that cause extreme blade loading. An extensive description of each flow regime is provided, with further investigation and discussion of the flow regimes that present more practical concerns and novel characteristics of the crashback flow.

iv

PUBLIC ABSTRACT

Propeller crashback is a common emergency slowing maneuver for ships and submarines. Reversing the propeller while the vessel is moving forward results in large loads on the blades and detached flow, presenting both practical concerns and fundamental fluid physics inquiries. This thesis presents a comprehensive numerical analysis of two propellers in crashback. Numerical and experimental data for David Taylor Model Basin (DTMB) 4381 propeller are used for validation of the fluid simulation code, REX. The Maritime Research Institute Netherlands (MARIN) 7371R propeller is used to classify common crashback flow behavior into regimes. Four regimes were identified, each existing for a range of operating conditions. The most prominent and deciding feature of the flow regimes is the presence of a ring vortex, resulting from the opposing free-stream flow and propeller induced flow. Its position, shape and strength change between regimes, dominating the dynamics of the flow into the propeller. Changes in the ring vortex structure lead to two stable flow conditions of interest: one with a reduction of thrust despite the increase in flow speed into the propeller and negligible side-forces, the other with large side-forces capable of rotating a vessel, resulting from an asymmetry forming in the ring vortex and massive flow separation at high free-stream speeds that cause extreme blade loading. An extensive description of each flow regime is provided, with further investigation and discussion of the flow regimes that present more practical concerns and novel characteristics of the crashback flow.

TABLE OF CONTENTS

vii

LIST OF TABLES

LIST OF FIGURES

xi

Chapter 1: Introduction/Motivation, Literature Review

1.1 Introduction/Motivation

Crashback operation is a critical design point for material failure of a marine propeller. This places great importance on the characterization of the forces exerted on the propeller during a crashback maneuver. There are four operating conditions for a propeller, each with their own quadrant in an open-water curve (OWC) (left Figure 1). An open-water curve is a plot of propeller thrust, torque and efficiency with respect to the operating advance coefficient (J), defined as the ratio between the free-stream velocity (U_o) and the product of the propeller's rotation rate (n, Hz) with its diameter (D):

$$J = \frac{U_o}{n \cdot D} \tag{Eq. 1}$$

Thrust coefficient K_T and torque coefficient K_Q are defined as follows:

$$K_T = \frac{T}{\rho n^2 D^4} \tag{Eq. 2}$$

$$K_Q = \frac{Q}{\rho n^2 D^5} \tag{Eq. 3}$$

where:
T is the thrust from the propeller (N)
Q is the torque from the propeller (N·m)
ρ is the density of water (kg/m^3)
n is the propeller rotation rate (Hz)
D is the propeller diameter (m)

The two operating conditions discussed in this document are the ahead and crashback conditions, represented as the first and third quadrant, respectively, in Figure 1. Crashback is the slowing maneuver for ahead operation, where positive free-stream velocity flows into the propeller disk due to the forward motion of the vessel and propeller rotational direction is negative, such that propeller thrust pushes against the incoming flow

(right Figure 1). These opposing motions cause high blade loading, leading to concern of sudden material failure or significant fatiguing of the blade material.

Another primary consequence of crashback are the side-forces acting on the propeller plane, produced by the recirculation of the propeller outflow. The high shear between the propeller induced flow opposing the free-stream flow generates the recirculation. These flow instabilities fall into different flow regime categories. The regimes range from a swirling round jet traveling upstream, a stable ring vortex formed just
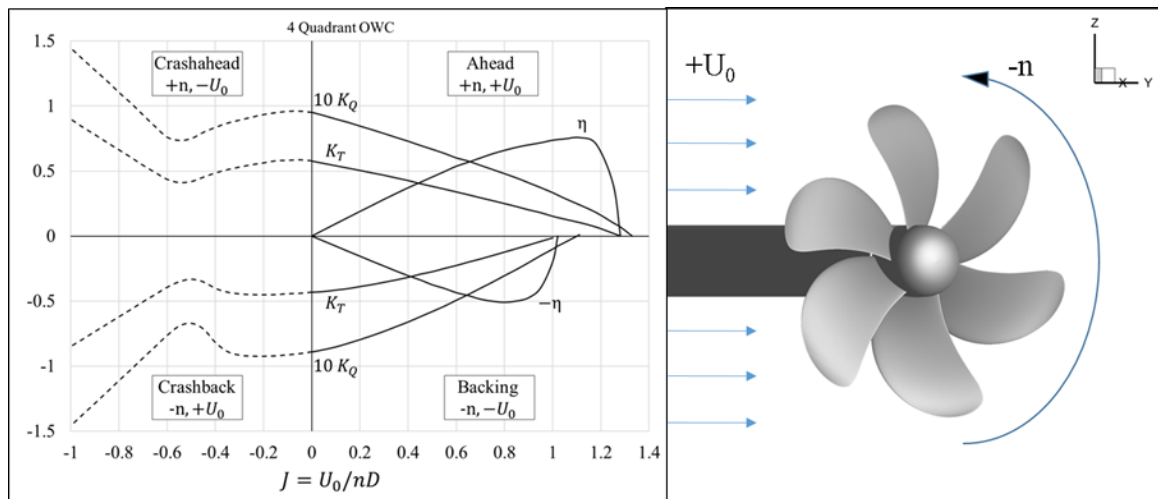
Figure 1: Four quadrants of a propeller OWC and sketch of crashback condition. Data for OWC (left) from Hecker and Remmers (1971). Propeller shown in crashback (right) is MARIN 7371R.

behind the propeller plane and a dispersed turbulent wake behind the propeller. A more detailed description of the flow regimes is included in other chapters. The side-forces acting on the propeller plane create low frequency, high amplitude moments at the center of gravity of the vessel. This will cause undesired motions, making it difficult to keep a specific orientation and trajectory when maneuvering.

1.2 Literature Review

1.2.1 Experimental investigations in crashback

An extensive tow tank experiment of propellers was performed by Hecker and Remmers (1971) to characterize the four quadrant performance of a range of propeller geometries. The propellers studied varied in the number of blades and blade shapes. The David Taylor Model Basin (DTMB) 4381 propeller, included in this document's investigation, was studied to collect torque and thrust data for all four quadrants of operation. An updated experiment of the 4381 in crashback was performed by Jiang et al. (1997) in the DTMB 24-inch Water Tunnel for advance coefficients of -0.472 and -0.732. Particle Image Velocimetry (PIV) measurements were taken to study the flow instabilities created during crashback. This experiment observed the formation of an unsteady ring vortex near the propeller blade tips downstream of the propeller. The ring vortex was observed moving away from the blade tips, wandering in a vertical and horizontal direction, returning to the location near the blade tips periodically. This periodic movement was matched to a low frequency harmonic exhibited in the time history of the transverse force acting on the propeller plane. Bursting of the ring vortex was also observed. A more recent experiment was performed on the 4381 propeller by Jessup et al. (2004) in the Naval Surface Warfare Center Carderock Division (NSWCCD) 36-inch variable pressure water tunnel (VPWT). Advance coefficients of -0.5 and -0.7 were examined. Thrust and torque were measured for OWC data comparison to Hecker and Remmers (1971) tow tank data. Particle image velocimetry (PIV) and laser Doppler velocimetry (LDV) were conducted to study the instabilities formed in the flow field that affect thrust and side-forces. A similar ring vortex formation was observed as was by Jiang et al. (1997). At the lower magnitude advance coefficient a more axisymmetric ring vortex structure was observed, with the swirl

3

of the propeller believed to induce swirl in the ring vortex. A smaller thrust value at this advance coefficient was attributed to smaller angles of attack. For the larger advance coefficient of -0.7, a more dominate radial flow was observed through the propeller disk creating large angles of attack believed to contribute to a higher thrust value. No obvious cyclic behavior of the ring vortex was observed as it was by Jiang et al. (1997). It is believed that this was due to differences in test section size. Large blade tip loading was associated with the ring vortex drifting inboard of the propeller tips, causing a large increase in reverse axial flow near the tips of the blades.

1.2.2 Numerical investigations in crashback

Early simulations of crashback used unsteady Reynolds Averaged Navier Stokes (RANS) solvers to compute the flow field. Zierke et al. (1997) simulated a fully appended submarine in a crashback maneuver using RANS coupled with a six degree of freedom (6DOF) solver. The formation of an asymmetric wobbling ring vortex was observed moving in and out of the propeller disk axially and wandering radially. A section of the ring vortex appeared attached to the blades at their tips while the diametrically opposed section was stretched radially away from the blade tips. A periodic low frequency in the side-forces acting on the propeller plane was observed, which produced the same periodic frequency in pitch and yaw of the submarine. As the submarine decelerated, the ring vortex became weaker and more axisymmetric about the propeller's axis of rotation. Although RANS showed its potential to qualitatively predict the flow behavior at different advance coefficients, large errors were reported by other RANS simulations comparing to experimental data. Chen and Stern (1998) reported a 110% error in the forces with respect to experimental data from Hecker and Remmers (1971), but only a 5% error in forward mode for the 4381 propeller. RANS was shown to not adequately predict the persistent

4

widespread unsteadiness of the flow field in crashback, resulting in large quantitative disagreement with experiments.

New methods were used to simulate crashback in order to capture this large-scale unsteadiness. Vyšohlíd and Mahesh (2006) performed a Large Eddy Simulation (LES) of 4381 at advance coefficients of 0.889 and -0.7. The computational domain was a simplified representation of the 36-inch VPWT as a cylindrical grid with the lateral edge of the domain positioned close to the propeller disk (3.65D from propeller centerline). Forward operation thrust and torque values showed very good agreement with Hecker and Remmers (1971) tow tank data, with water tunnel data from Jessup et al. (2004) and Jessup's tow tank data reported by Vyšohlíd and Mahesh (private communication to Vyšohlíd & Mahesh) under predicting the thrust and torque of the propeller. For crashback operation, LES thrust and torque values fell between Jessup et al. (2004) water tunnel values and the reported Jessup tow tank values. Values for thrust and torque predicted by Hecker and Remmers (1971) tow tank experiment were significantly larger in magnitude, as much as 25% larger than the values predicted by the reported Jessup tow tank experiment. The formation of a wandering unsteady ring vortex behind the propeller disk near the blade tips was observed. No clear low frequency harmonic was seen in the time history of the side-forces as was seen by Jiang et al. (1997) and Zierke et al. (1997). Circumferentially-averaged flow field solutions were compared to Jessup et al. (2004) PIV water tunnel flow measurements. Good agreement was shown for axial root-mean square (RMS) velocities near the ring vortex and propeller plane. Significant differences were shown in the radial and tangential velocities of the flow field in the area near the ring vortex. Chang et al. (2008) expanded the investigation with the same LES code to include advance coefficients of -0.3, -0.5 and -1.0

5

in addition to -0.7. All advance coefficients were run for more rotations than the investigation by Vyšohlíd and Mahesh (2006) to improve the statistics of the unsteady crashback flow fields. The analysis was focused on advance coefficients -0.5 and -1.0, since these operation points were thought to span the spectrum of flow behavior with a ring vortex present. Thrust and torque values for LES at $J = -0.5$ and -0.7 fell between values from Jessup et al. (2004) VPWT values and Hecker and Remmers (1971) tow tank data. $J = -0.3$ and -1.0 values agree better with Hecker and Remmers (1971) tow tank data. Resultant side-force was computed and compared to tow tank and water tunnel data. LES results matched better to water tunnel data throughout the range of advance coefficients simulated. A significant observation is the difference in resultant side-forces between water tunnel and tow tank data. For advance coefficients greater than or equal to -0.5 (in magnitude) tow tank side-force values are consistently higher than water tunnel values. The trend for the tow tank data shows an exponential distribution with a maximum side-force value occurring near $J = -1.2$. Water tunnel side-force data does not exhibit an exponential behavior, remaining approximately linear reporting small side-force values even at $J = -1.2$. This difference contends that experimental conditions and design significantly affect flow field features, such as the ring vortex, and therefore the side-forces produced by the propeller. Power Spectral Density (PSD) distributions agreed well to VPWT data by Jessup et al. (2004) for advance coefficients greater than or equal to -0.5 up to the blade passage frequency (BPF). The PSD distribution for $J = -0.3$ did not compare well to VPWT data in magnitude, but the overall trend followed experimental data. Beyond the BPF, the LES simulations did not capture the same energy scales as the experiment, but a frequency near twice the BPF was captured for all simulations except $J = -1.0$. The instantaneous flow

6

fields for J = -0.5 and -1.0 were analyzed to investigate major events in the time histories for thrust and side-forces. These large spikes and drops in the forces were associated with specific deformations of the ring vortex and accumulation of turbulent structures near the surface of the blades. For J = -0.5 a large spike in thrust and resultant side-force was associated with the stable, axisymmetric ring vortex deforming into a round jet that traveled upstream of the propeller (relative to free-stream velocity) and accumulation of turbulent structures near the surface of the blades, respectively. However, this event was shown to be uncommon by the probability density functions (PDF) for thrust and resultant side-force, lying 4.9σ from the mean thrust value. A time point of minimum thrust and resultant side-force was shown to occur when the ring vortex was strongly axisymmetric, creating a highly uniform inflow into the propeller. There was less accumulation of turbulent structures near the surface of the blades, believed to cause the drop in side-force. For J = -1.0, the same explanation was given its time history where thrust and side-force were small. The high amplitude event analyzed showed that the free-stream was able to flow into the propeller plane near the root of a portion of the propeller disk's circumference causing high angles of attack (AoA), resulting in an increase in thrust and side-force values. It was concluded that the difference in setup between the water tunnel and open-water (OW) tow tank experiments may have two factors causing differences in predicted forces. It was suggested that the shaft located behind the propeller for the OW experiment slowed down the flow being ingested by the propeller, and the absence of the shaft upstream allowed the free-stream flow in front of the propeller to enter the propeller disk more freely near the blade roots. This is believed to exacerbate the side-forces and cause differences in thrust levels between the two experimental setups. Jessup et al. (2006) noted, after performing a

7

study on a ducted and un-ducted propeller in crashback, that the ring vortex produced in crashback reaches far enough into the free-stream where a shear layer is present, formed by the water tunnel nozzle. The interaction with the shear layer may create large effects on ring vortex behavior that are not generated in the open-water conditions of the tow tank.

Chapter 2: Numerical Methods, CFD Code REX

REX is a proprietary unsteady Reynolds-Averaged Navier-Stokes (URANS) CFD solver with capabilities for detached eddy simulation (DES) and delayed detached eddy simulation (DDES), continually developed by Pablo Carrica's Research Group (PCRG) at the University of Iowa.

Continuity and momentum conservation are enforced using the following non-dimensionalized equations. The equations are non-dimensionalized using a reference velocity U_o (chosen as ship velocity, experimental tunnel velocity, etc.) and characteristic length L (ship/submarine length, propeller radius, etc.):

$$\frac{\partial u_j}{\partial x_j} = 0 \tag{Eq. 4}$$

$$\frac{\partial u_i}{\partial t} + \frac{\partial u_i \partial u_j}{\partial x_j} = -\frac{\partial p}{\partial x_i} + \frac{\partial}{\partial x_j}\left[\frac{1}{Re_{eff}}\left(\frac{\partial u_i}{\partial x_j} + \frac{\partial u_j}{\partial x_i}\right)\right] + s_i \tag{Eq. 5}$$

where:

$p = \frac{p_{abs}}{\rho U_o{}^2} + \frac{2k}{3}$ is the dimensionless piezometric pressure

$\boldsymbol{p_{abs}}$ is the absolute pressure

$\boldsymbol{k}$ is the turbulent kinetic energy (TKE)

$\frac{1}{\boldsymbol{Re_{eff}}} = \frac{1}{R_e} + \nu_t$ is the effective Reynolds number

$\boldsymbol{\nu_t}$ is the turbulent viscosity determined by the turbulence model

$\boldsymbol{s_i}$ is the source term

The URANS equations are solved for either laminar flow or turbulent flow, with turbulence modeled typically by isotropic Menter's blended k-ω/k-ε (Menter, 1994). The equations for the model are:

$$\frac{\partial k}{\partial t} + \left(u_j - \sigma_k \frac{\partial \nu_t}{\partial x_j}\right)\frac{\partial k}{\partial x_j} - \frac{1}{P_k}\frac{\partial^2 k}{\partial x^2{}_j} + s_k = 0 \tag{Eq. 6}$$

$$\frac{\partial \omega}{\partial t} + \left(u_j - \sigma_\omega \frac{\partial \nu_t}{\partial x_j}\right)\frac{\partial \omega}{\partial x_j} - \frac{1}{P_k}\frac{\partial^2 \omega}{\partial x^2{}_j} + s_\omega = 0 \tag{Eq. 7}$$

9

where k is the turbulent kinetic energy (TKE) and ω the specific dissipation rate, with the turbulent viscosity defined as $v_t = k/\omega$. The Peclet numbers are defined as:

$$P_k = \frac{1}{\frac{1}{Re}+\sigma_k v_t} \, , \, P_\omega = \frac{1}{\frac{1}{Re}+\sigma_\omega v_t} \tag{Eq. 8}$$

The source for k and ω are defined as:

$$s_k = -G + \beta^* \omega k \tag{Eq. 9}$$

$$s_\omega = \omega\left(\beta^* \omega - \gamma \frac{G}{k}\right) - 2(1-F_1)\sigma_{\omega 2}\left(\frac{\partial k}{\partial x_j}\right)\left(\frac{\partial \omega}{\partial x_j}\right)\frac{1}{\omega} \tag{Eq. 10}$$

where:

$$G = v_t \tau : \left(\frac{\partial u_i}{\partial x_j}\right) \tag{Eq. 11}$$

$$F_1 = \tanh\left[\left(min\left(max\left(\frac{\sqrt{k}}{0.09\omega\delta}; \frac{1}{Re}\frac{500}{\delta^2\omega}\right); \frac{4\sigma_{\omega 2}k}{CD_{k\omega}\delta^2}\right)\right)^4\right] \tag{Eq. 12}$$

$$CD_{k\omega} = \max\left(2\sigma_{\omega 2}\frac{1}{\omega}\left(\frac{\partial k}{\partial x_j}\right)\left(\frac{\partial \omega}{\partial x_j}\right); \, 10^{-20}\right) \tag{Eq. 13}$$

In the wake region, the blending function F_1 is zero and switches to one in the logarithmic and sublayer regions of the boundary layer. The distance to the closest no-slip surface, δ, is needed to calculate F_1.

An SST model is an available option that accounts for turbulent stress transport. This is useful to improve results for flows with adverse pressure gradients. The model differs from Menter's blended model by using the absolute value of the vorticity, Ω, to define the turbulent viscosity as:

$$v_t = \frac{0.31k}{\max(0.31\omega; \Omega F_2)} \tag{Eq. 14}$$

$$F_2 = \tanh\left[\left(max\left(\frac{2\sqrt{k}}{0.09\omega\delta}; \frac{500v}{\delta^2\omega}\right)\right)^2\right] \tag{Eq. 15}$$

10

For massively separated flows, turbulence can be modeled using k-ω/k-ε based detached eddy simulation (DES) and delayed DES (DDES). The dissipative term of the k-transport equation is replaced with:

$$D_{RANS}^k = \rho \beta^* k \omega = \frac{\rho k^{\frac{3}{2}}}{l_{k-\omega}} \tag{Eq. 16}$$

$$D_{DES}^k = \rho \frac{k^{\frac{3}{2}}}{l} \tag{Eq. 17}$$

where the length scales are defined as:

$$l_{k-\omega} = \frac{k^{\frac{1}{2}}}{\beta^* \omega} \tag{Eq. 18}$$

$$\tilde{l} = \min(l_{k-\omega}, C_{DES}\Delta) \tag{Eq. 19}$$

$C_{DES} = 0.65$ and Δ is the local grid spacing. This model determines where RANS or LES is applied. A more detailed explanation of DES and DDES models can be found in Xing et al. (2007) and Xing et al. (2010), respectively.

REX uses generalized curvilinear coordinates allowing for body-fitted structured grids. Overset grids are used, with their overlap and domain connectivity information (DCI) computed by the codes Suggar or Suggar++ (Noack & Boger, 2009). This allows for relative motion between grids and modeling of solid bodies including appendages using composite grid systems.

Motions are implemented using a hierarchy of bodies (Carrica et al., 2007b) by computing rigid body equations for the parent body (submarine, ship) in a six degrees of freedom (6DOF) solver, and using controllers or imposed input motions to allow the appendages (rudders, propellers, stabilizers, etc.) to move in one degree of freedom with respect to the parent body. REX has several Proportional-Integral-Derivative (PID) controllers enabling simulation of self-propulsion, maneuvers, autopilot, deployment and

11

recapturing of UUVs, etc. More detail of the functionality of the controllers can be found in Carrica et al. (2008). Propellers can be represented in REX using the discrete geometry of the blades, body force models such as Hough and Ordway (1965), or by coupling a third-party solver, such as the potential flow solver PUF-14 (Kerwin et al., 1987). Using a potential flow model significantly reduces computational cost while maintaining good agreement with experimental and fully-discretized results (Martin et al., 2015).

More advance multi-body dynamic simulations are possible including cable connections between bodies. Fluid-structure interaction problems can be simulated for flexible bodies using a modal analysis outputted by a code like ANSYS or Abaqus (Paik et al., 2009). One-way or two-way coupling is possible. Modeling of nonlinear deformations are done with an internal solver or by coupling REX to the multibody solver Virtual Lab (Y. Li et al., 2015).

REX uses a single-phase level set approach to model free surface flows (Carrica et al., 2007a). REX can compute a two phase air/water free surface interface using a semi-coupled method where the water free surface is decoupled from the air computation. The air computation uses the unsteady water free surface as an immersed boundary condition Huang et al. (2008). A two-way coupled polydisperse model is used to simulate bubbly two-phase flows based on Boltzmann theory of gases. The polydisperse model solves for the continuous phase (water) velocities and pressure and then performs the calculations for a statistically described distribution of bubbles. The Boltzmann-like equation includes effects related to bubble transport and intergroup transfer such as breakup, coalescence and dissolution (J. Li et al., 2015). Stratified flows are modeled using the Boussinesq approximation detailed in Esmaeilpour et al. (2016).

12

REX is intended for high-Reynolds number flows, causing the transport and reinitialization equations to be weakly elliptical and thus enabling pentadiagonal line solvers in an alternate-direction-implicit (ADI) scheme to be used. Parallel processing is enabled by use of an MPI-based domain decomposition, where each decomposed block is mapped to one processor. Inter-processor information transfer is made after each ADI iteration and boundary condition enforcement. The matrix for pressure includes the information of the multi-block overset interpolation and boundary conditions. The pressure Poisson equation is solved using a multigrid-preconditioned Krylov solver from the PETSc library (Yang et al., 2007).

13

Chapter 3: Simulation Design and Setup

The broad analysis of crashback is performed using a medium grid for Maritime Research Institute Netherlands (MARIN) 7371R propeller. A medium grid for DTMB 4381 was run for validation with experiment and other numerical methods.

3.1 Grid Design

Crashback analysis was performed on the DTMB 4381 and MARIN 7371R propellers, pictured in Figure 2 below. 4381 is a five-bladed neutral skew and rake variable pitch propeller with a model scale diameter of 12 inches. Its shaft design was based on the shaft used in the 36-inch VPWT experiment, with the shaft and hub being one continuous geometry for the simulation. 7371R is a six-bladed high skew submarine propeller used in free-running experiments by MARIN for the submarine geometry Joubert BB2 with a model scale diameter of 10.73 inches. Its shaft design is a generic shaft with no reference to an experimental geometry. The separate hub is the same hub used in simulations of Joubert BB2 in self-propulsion and maneuvering (Carrica et al., 2016).
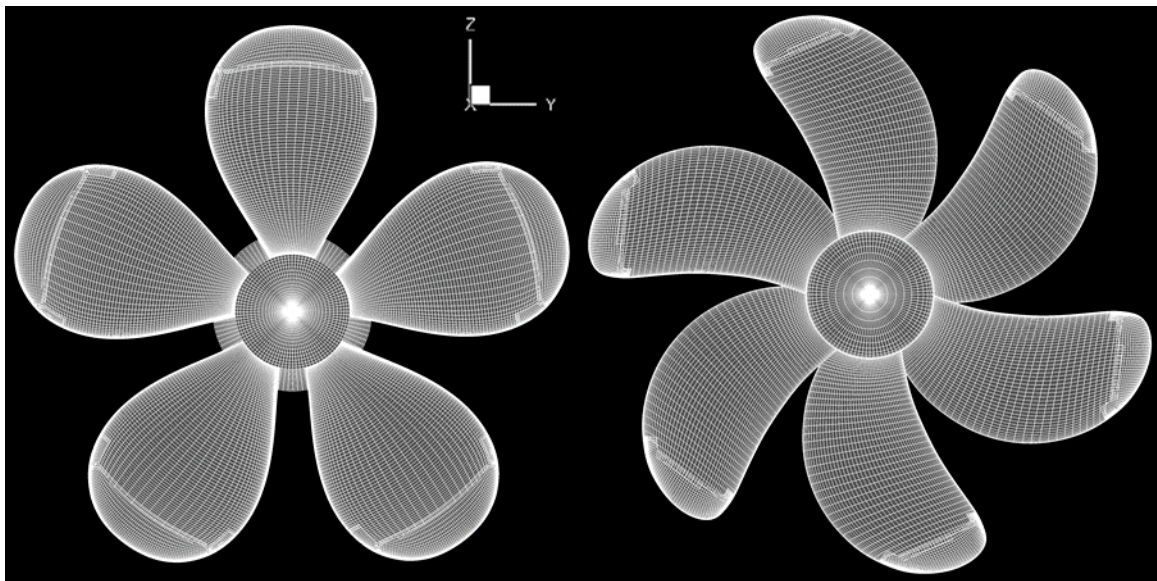
Figure 2: Geometry and surface grids for the shaft, hub and blades of 4381 & 7371R.DTMB 4381 (left) and MARIN 7371R (right).

14

REX CFD code uses structured overset grids. Shown in Figure 2, the blades of the propellers were discretized using the traditional method for ahead operation studies of two overlapping grids. A finer grid is used for the blade tips to capture blade tip vorticity. Shaft/hub grids were designed to be coarse in regions away from the propeller disk, with a refinement bias centered in the middle of the propeller disk. Points far upstream from the propeller are less critical since the flow is highly attached and uniform. The same refinement and background grids were used for both propellers. A Cartesian refinement grid was used to capture a broad spectrum of turbulent structures near the propeller disk (left Figure 3 below). The refinement grid covered a large region around the propeller since major flow features are produced in front or behind the propeller depending on the operating advance coefficient. The refinement grid contained a region two and a half propeller diameters (D, based on 7371R) in length, height and width centered on the propeller disk, set to equal spacing of 0.00969D (medium grids). The equal spacing region
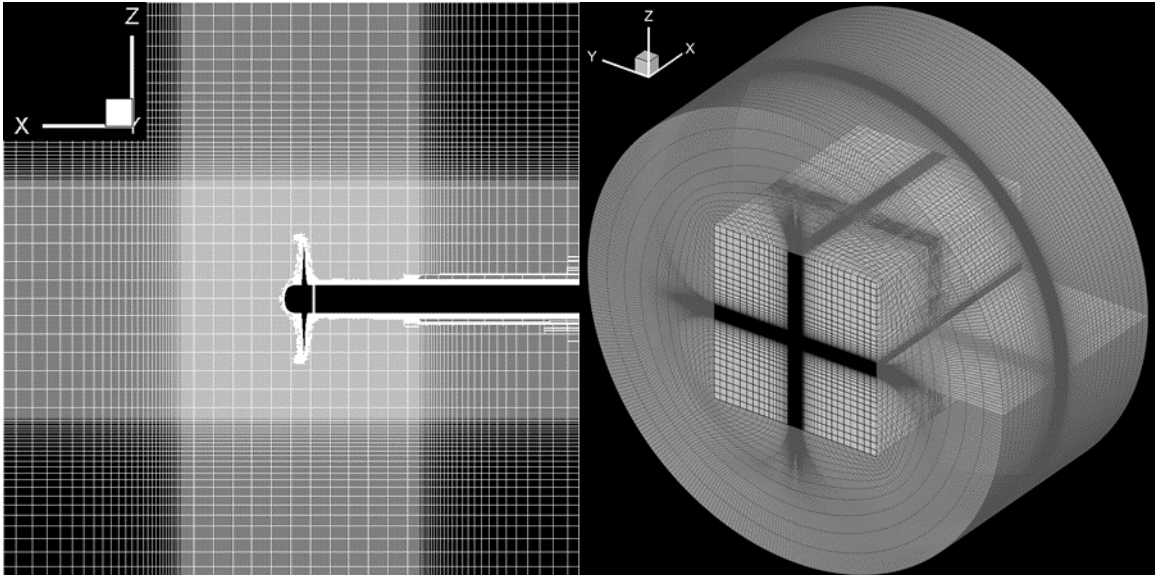
Figure 3: Propeller refinement grid and background grid design. The refinement grid (left) and the background grid with cylindrical sleeve grid (right) were used for both propeller geometries.

was hyperbolically coarsened to a maximum grid spacing 0.1534D at the edges of the refinement grid.

The background grid was constructed with two separate grids. An unmodified Cartesian background grid was originally used, but early test simulations showed issues with the pressure field causing spurious fluxes on the faces of the lateral boundary conditions and at the sharp corners of the grid (since all grids including the background grid were rotated together, as it is explained below in Section 3.2). To resolve these issues a cylindrical sleeve grid was constructed such that the distance to the lateral boundary was extended and no sharp corners were present on the lateral boundary condition that would cause spurious fluxes. The two background grids share common grid points at their interface, pictured on the right of Figure 3. The final dimensions of the combined background grid from the center of the propeller disk are 38.3D to the inlet boundary, 56.4D to the outlet boundary and 98.3D to the lateral cylindrical boundary. Table 1 contains a summary of the grid dimensions for each grid system used. The 7371R medium grid system was coarsened and refined by a factor of $\sqrt{2}$ in each direction to obtain a coarse and fine grid, respectively. A grid study for flow behavior and force convergence was performed using these grids. The shaft and hub were not coarsened for the coarsest grid to prevent poor overset quality to the blade, refinement and background grids. These grids are of little concern apart from the refinement level for the boundary layer.

Table 1: Grid System Sizes: 4381 and 7371R Medium Grid, 7371R Coarse Grid, 7371R Fine Grid

Grid size: million (M)	Shaft	Hub	Blade	Blade Tip	Refine	Bkgrnd Cart	Bkgrnd Cyl	Total
4381	1.0395M	-	0.50106M	0.2526M	15.81M	-	1.831M	23.9M
7371R	0.7243M	0.1597M	0.1597M	0.08063M	15.81M	1.234M	0.6308M	21.48M
7371R Coarse	0.7243M	0.1597M	0.05623M	0.02851M	5.545M	0.4285M	0.2150M	8.328M
7371R Fine	1.988M	0.4305M	0.4305M	0.2168M	43.24M	3.400M	1.827M	59.61M

16

3.2 Case Setup and Methodology

The grid overset connectivity was computed using the third-party code Suggar as a pre-processing step, such that a static overset was used throughout a computation. Since the grids are not allowed to move relative to one another, the rotational motion of the propeller was simulated by rotating the entire grid system at the rotational rate of the propeller. To compute the forces on the propeller blades and hub only (to replicate the dynamometer in the experiment) surface IDs were assigned to the surface cells of each blade and the hub. This allowed for per blade analysis and the total forces to be computed excluding the contributions from the shaft.

For 7371R the rotational speed used was 15 Hz based on experimental data (private communication). A length and velocity scale was chosen to non-dimensionalize the geometry and flow field variables computed during the simulation. A length scale of 3.826m was chosen, corresponding to Joubert BB2 model scale from experiments performed by MARIN (Overpelt, 2015). The velocity scale was based on the free-stream flow velocity of the experimental straight ahead case run at J = 1.0, the highest advance coefficient run experimentally. This corresponds to a velocity scale that is the product of the propeller rotational speed and the propeller diameter:

$$J = \frac{U_o}{n \cdot D} = 1.0 \ \rightarrow U_o = n \cdot D$$

Using the velocity and length scale the Reynolds number was computed as:

$$R_e = \frac{U_S \cdot L_S}{\nu} = \frac{(n \cdot D) \cdot L_S}{\nu} \tag{Eq. 20}$$

where:
U_s is velocity scale corresponding to J = 1 (m/s)
L_s is length scale chosen as overall length of BB2, model scale (m)
ν is kinematic viscosity of freshwater at 20˚C (m²/s)
n is the experimental rotational speed of the propeller (Hz)
D is propeller diameter, model scale (m)

17

Therefore, the Reynolds number for 7371R is computed as:

$$R_e = \frac{(15 \cdot 0.27251) \cdot 3.826}{1E-6} = 15.639E6$$

To change the advance coefficient for 7371R, the rotational speed was kept constant while the inlet velocity was changed. For 4381, both the inlet velocity and rotational speed were changed to obtain the correct advance coefficient. A Reynolds number reported by Chang et al. (2008) and Jessup et al. (2004) of 480,000 was used. The propeller radius (used as the length scale for 4381) and the Reynolds number were used to compute a velocity scale:

$$R_{e,r} = \frac{U_{s,4381} \cdot R_{4381}}{\nu} \rightarrow U_{s,4381} = \frac{R_{e,R} \cdot \nu}{R_{4381}}$$

where:
$U_{s,4381}$ is the velocity scale for 4381 cases (m/s)
R_{4381} is the radius of 4381 propeller at model scale (m)
ν is the kinematic viscosity of freshwater at 20˚C (m^2/s)

The velocity scale for 4381 is then,

$$U_{s,4381} = \frac{480,000 \cdot 1E-6}{0.1524} = 3.150 \; m/s$$

Inlet velocities and rotational speeds were based on values reported in Jessup et al. (2004) and Chang et al. (2008), shown in Table 2 below. Note that J = -0.6 was not run either experimentally in the water tunnel or computationally in LES simulations. The

Table 2: Propeller speeds and free-stream velocities 4381

J	n (RPM)	n (RPS)	U_o, VPWT (m/s)
0.3	660	11	1.006
-0.3	-700	-11.6667	1.067
-0.5	-700	-11.6667	1.778
-0.6	-600	-10	1.831
-0.7	-600	-10	2.134
Jessup et al. (2004)	Chang et al. (2008)		

rotational speed and inlet velocity were non-dimensionalized using the velocity and length scale. Time steps were chosen so that the propeller performed one degree of rotation per time step.

Simulations for 4381 and 7371R were run using DDES with fourth order upwind convection term using hybrid discretization. The hybrid method uses second order for distances up to twice a small distance specified in the input. Any greater distance is computed with a fourth order scheme. Each case was run for a minimum of 150 propeller rotations. For validation, both propellers were run in straight ahead condition to compare to experimental data. 4381 was run in crashback condition at the advance coefficients listed in Table 2, comparing the water tunnel experiment by Jessup et al. (2004), LES simulations performed by Chang et al. (2008) and updated experimental open-water data by Ebert et al. (2007). Side-forces for 4381 were compared to open-water data from Hecker and Remmers (1971) and water tunnel data by Jessup et al. (2004). No experimental open-water data is available for 7371R in steady-state crashback. However, experiments were performed for a free-running model of the Joubert BB2 submarine geometry equipped with the MARIN 7371R propeller (Overpelt, 2015). Simulations at model scale using REX were performed for numerical validation (Carrica et al., 2016). The end of a surfacing maneuver studied included a crashback phase to stop the submarine. The time history of the transient experiment and simulation were used to perform a rough comparison to steady-state DDES results completed for this analysis. Advance coefficients from $J = -0.2$ to -1.0 with a delta of -0.1, -1.5 and -2.0 were run in crashback to fully characterize the OWC in the third quadrant for 7371R. Additionally for 7371R, advance coefficients of $J = -0.3$ to -1.0 with a delta of -0.1, -1.0 and -1.5 were simulated with 10˚ of flow angle from the port side to

19

study the effects of oblique flow on crashback. No experimental data is available for oblique flow in crashback operation. Computations were performed using Department of Defense (DoD) High Performance Computing (HPC) machines.

20

Chapter 4: Results and Discussion

4.1 Validation with Open-Water and Water Tunnel, Straight Ahead and Crashback Operation

The first quadrant containing 4381 and 7371R ahead data and the third quadrant containing 4381 crashback data are presented in Figure 4 below. The first quadrant on top compares thrust and torque coefficient results between experimental data and REX DDES results for 4381 (open symbols) and 7371R (solid symbols). Experimental data for 4381 (dash-dot lines) is from tow tank data by Hecker and Remmers (1971) and 7371R experimental data (solid lines) is shown as reported in Pontarelli et al. (2017).

Thrust is slightly under-predicted while torque is slightly over-predicted for both propellers in straight ahead operation. Overall the simulation results are in excellent agreement with experimental results for ahead operation. Experimental 4381 crashback data from Jessup et al. (2004) water tunnel (dashed lines) and Ebert et al. (2007) tow tank (dotted lines) are shown on the bottom of Figure 4, respectively. Overall, average steady-state simulation values fall between water

Figure 4: Validation of OWC with experiment for 7371R & 4381 in ahead operation and 4381 only in crashback operation. Simulation results (symbols), experimental results (lines). DTMB 4381 (open symbols) and MARIN 7371R (solid symbols). 7371R ahead open-water data as reported in Pontarelli et al. (2017) (solid lines), 4381 open-water data from Hecker and Remmers (1971) (dash-dot lines). 4381 crashback data from Jessup et al. (2004) water tunnel (dash lines) and Ebert et al. (2007) open-water (dotted lines).

tunnel and open-water experimental values. DDES simulation results should be more consistent with open-water values since the computational domain better approximates

open-water conditions versus water tunnel conditions. This is primarily true for thrust and torque values, but J = -0.6 shows a deviation from this trend towards water tunnel values.

As stated in Section 1.2, clear differences were seen between tow tank experiment, 36-inch water tunnel experiment and LES water tunnel simulation results for thrust and particularly for resultant side-force. Side-force magnitude coefficient is defined as the resultant of the horizontal and vertical force:

$$K_s = \sqrt{K_{Ty} + K_{Tz}} \qquad \text{(Eq. 21)}$$

where the horizontal and vertical side-force coefficients are:

$$K_{Ty} = \frac{F_y}{\rho n^2 D^4} \qquad \text{(Eq. 22)}$$

$$K_{Tz} = \frac{F_z}{\rho n^2 D^4} \qquad \text{(Eq. 23)}$$

where:
F_y is the horizontal force from the propeller (N)
F_z is the vertical force from the propeller (N)
ρ is the density of water (kg/m^3)
n is the propeller rotation rate (Hz)
D is the propeller diameter (m)

Figure 5 shows a comparison of resultant side-force values between Jessup et al. (2004) VPWT data, Hecker and Remmers (1971) open-water data, LES data by Chang et al. (2008) and DDES REX data. VPWT side-force data shows a peak at J = -0.3 followed by a gradual decrease until J = -0.5 and a gradual increase for increasingly negative J. Open-water side-force data continuously increases until J = -0.5 when it stays nearly constant until J = -0.7, at which point it rapidly increases to a peak at approximately J = -1.1. After the peak in side-forces, it appears to asymptotically decrease to a constant side-force value for a sufficiently high advance coefficient. As stated in Section 1.2, differences in side-force results were attributed to water tunnel nozzle and wall effects as well as influences

22

of shaft position on flow into the propeller. The domain of the LES simulations resembles the experimental fluid domain of the VPWT setup, while the fluid domain for DDES simulations approximates experimental conditions of open-water tests by Hecker and Remmers (1971). However, simulation results show a changing trend in agreement with a certain experimental setup. DDES resembles LES and open-water data for $J = -0.3$.
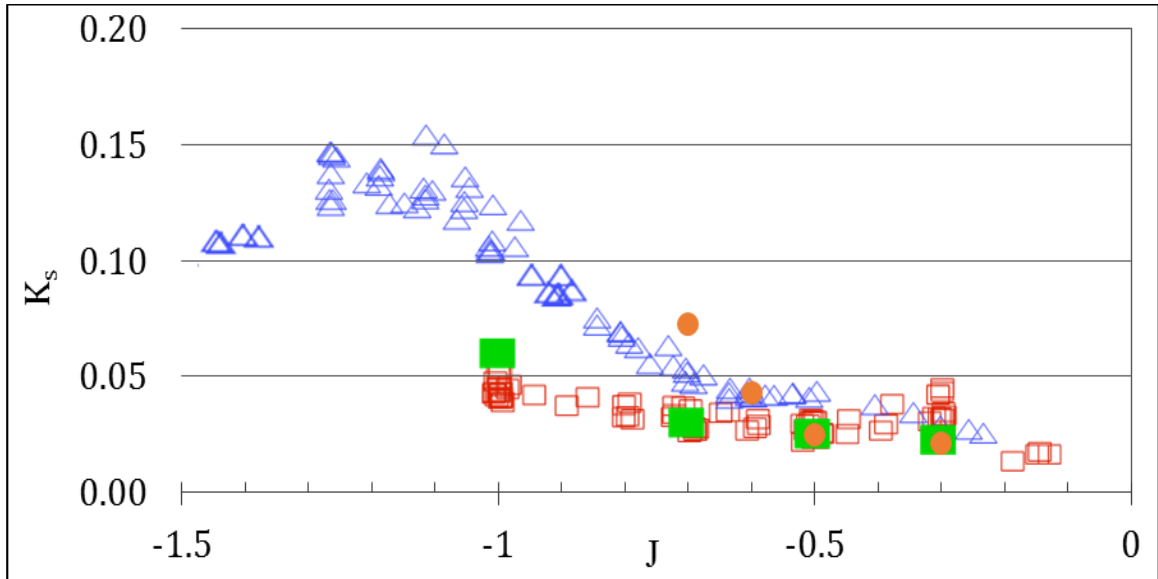
Figure 5: Validation of resultant side-force coefficient (K_S) with experiments and LES for 4381 in crashback. △ : Hecker and Remmers (1971) open-water data. □ : Jessup et al. (2004) VPWT data. ■ : Chang et al. (2008) LES results. ● : REX DDES results.

Sufficiently low magnitude advance coefficients produce a large upstream traveling jet. This jet would likely cause blockage of the flow out of the narrow water tunnel nozzle in the experiment. Since the LES, DDES and open-water experiment domains do not include this narrow passage close to the propeller disk, flow blockage effects would be smaller. DDES is in parity with LES and water tunnel results for $J = -0.5$. At this advance coefficient, thrust and torque achieve a minimum due to the tight area of recirculation of the propeller induced flow. The area of influence of the propeller recirculation would not reach far enough to significantly interact with the external geometry farther from the propeller disk (e.g. the water tunnel nozzle). However, shaft position would affect the

velocities at the inflow and outflow plane of the propeller disk. All shaft geometries are the same except for open-water, which has a downstream shaft typical for tow tank experiments. Hence, LES, DDES and VPWT values are very similar. For more negative advance coefficients, LES results match better with VPWT data. At advance coefficients with magnitudes greater than $J = -0.5$, flow output from the propeller disk sees a significant increase in radial and tangential flow due to asymmetry of the ring vortex induced flow. If wall effects, tunnel nozzle shear layer effects and shaft location influence ring vortex behavior and therefore its induced flow, large differences in the side-forces would be introduced. The asymmetry of the ring vortex is associated with the increase in thrust and side-forces from smaller values at lower magnitude advance coefficients. This ring vortex is present for a narrow operating range of 4381 and is sensitive to transient changes in the flow field. If the ring vortex were to shift to a lower advance coefficient behavior where forces are smaller, this would affect the average taken over time. As expressed in section 1.2.2, it was speculated that the shear layer of the water tunnel nozzle would interact with the larger radius ring vortex at higher magnitude advance coefficients. Comparatively, the lateral boundaries of the LES simulations lie only 3.65 diameters away from the propeller disk centerline, and are modeled to act like a wall boundary. Crashback produces an immense pressure field that necessitates larger radial distances before pressure gradients are minimal.

To explore these differences further, probability density functions (PDFs) were produced for thrust coefficient K_T and side-force coefficient K_s. A comparison is drawn between Jessup et al. (2004) VPWT data, Chang et al. (2008) LES results and REX DDES results in Figure 6 below. PDFs for $J = -0.3$ (top) and $J = -0.5$ (middle) confirm the relative

24

comparisons for side-force in Figure 5. For J = -0.3, DDES results show strong agreement

with LES data for side-forces, but VPWT results differ significantly for side-force from

simulations. Both simulation methods and VPWT agree well for thrust at J = -0.3. At J = -

0.5 both simulation methods and VPWT show parity for thrust and side-force. At the largest

advance coefficient of J = -0.7, DDES results display a small but increased disagreement

in thrust with LES and VPWT results, but a large disagreement with VPWT and LES for
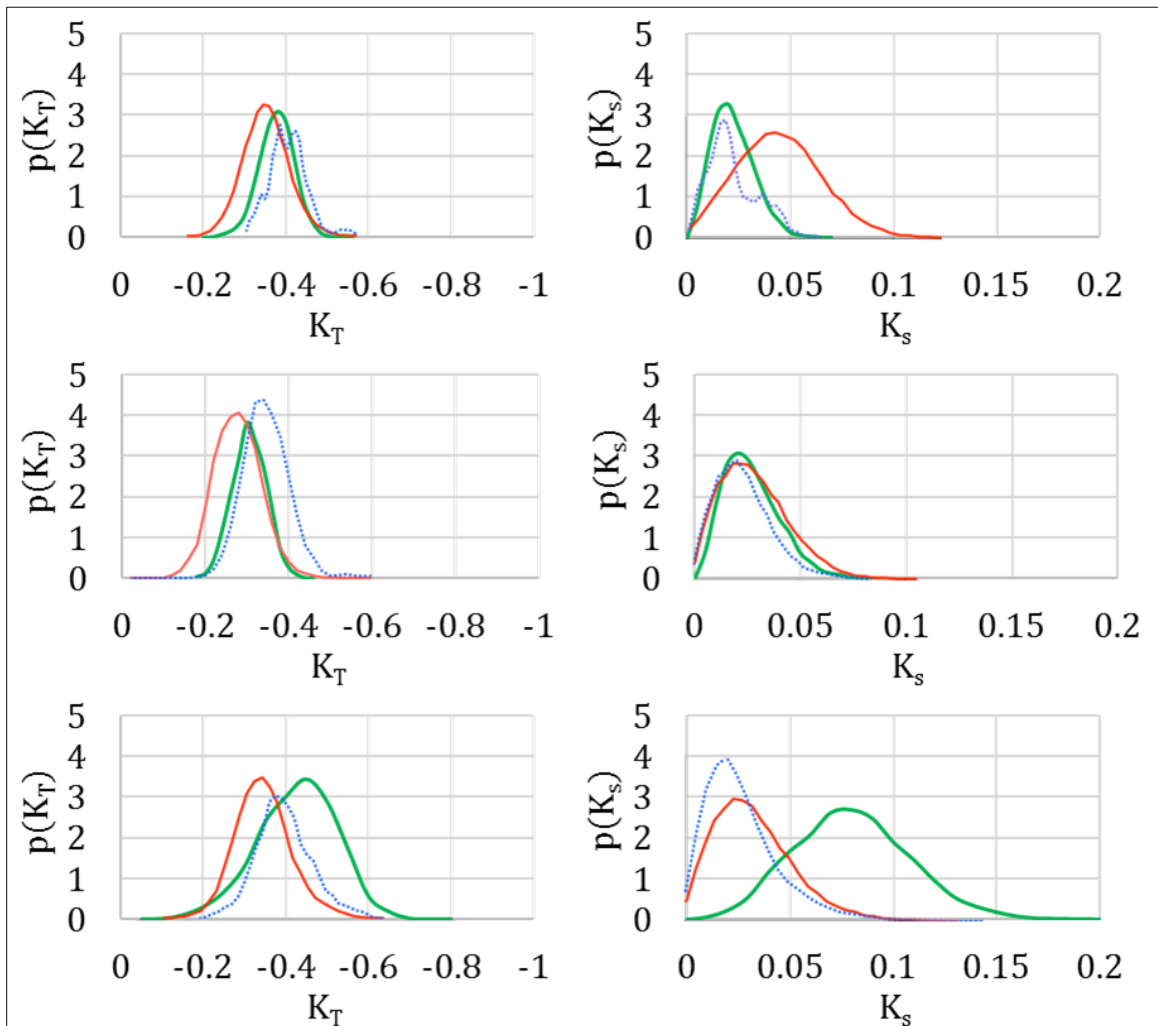
Figure 6: Validation of probability density functions for thrust (K_T) and resultant side-force (K_S) coefficient with experimental and LES results for 4381 in crashback. J = -0.3 (top), J = -0.5 (middle), J = -0.7 (bottom). Jessup et al. (2004) VPWT data (red). Chang et al. (2008) LES (blue-dotted). REX DDES data (green).

25

side-force. Time history data for open-water experiment was not available but it is believed that a PDF of OW data would exhibit better agreement with DDES results.

Power-spectral density (PSD) plots of the forces reveal dominant frequencies and their relative energy content, which characterize the differences in resolved and measured flow fields. Figure 7 contains propeller 4381 PSDs of side-force magnitude for J = -0.3 and -0.5. Figure 8 contains propeller 4381 PSDs of side-force magnitude and thrust for J =-0.7 only. DDES values are compared to results from Jessup et al. (2004) for VPWT and Chang et al. (2008) for LES at advance coefficients J = -0.3 and -0.5. For J = -0.7, PSD values are compared to Jessup et al. (2004) VWPT data and finer grid LES results reported by Jang
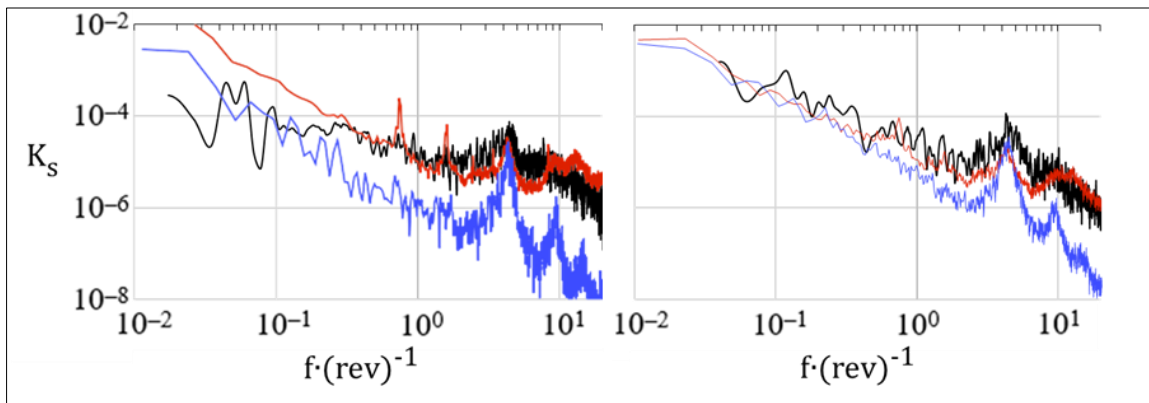
Figure 7: Validation of PSDs for resultant side-force (K_S) coefficient with experiment and LES for 4381 in crashback, J = -0.3, -0.5. J = -0.3 (left), -0.5 (right). Black line DDES REX, blue line Chang et al. (2008) LES, red line Jessup et al. (2004) VPWT. Frequencies normalized by propeller rotational speed.
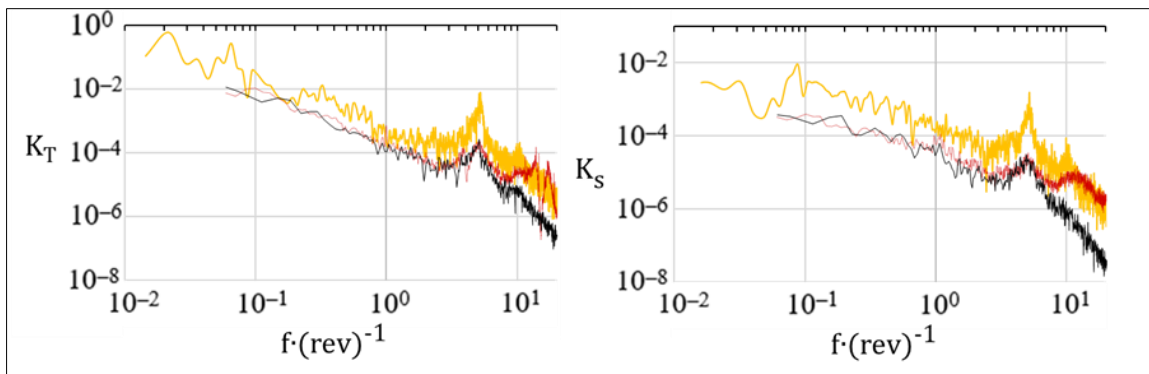
Figure 8: Validation of PSDs for thrust (K_T) and resultant side-force (K_S) coefficient with experiment and LES for 4381 in crashback, J = -0.7. Gold line DDES REX, black line Jang and Mahesh (2013) LES, red line Jessup et al. (2004) VPWT. Frequencies are normalized by propeller rotational speed.

26

and Mahesh. (2013). For the smaller advance coefficients of J = -0.3 and -0.5, DDES results displays strong agreement with Jessup et al. (2004) VPWT experimental results. Experimental results show lower frequency harmonics below blade passage frequency (BPF). This was attributed to frequencies of the dynamometer assembly. Chang et al. (2008) LES results, experimental and DDES results display a strong harmonic at the BPF, however, LES results contain harmonics at twice BPF and higher for J = -0.3 and -0.5. For J = -0.7 DDES results have slightly higher energy content which is to be expected because of the higher average KT and Ks values that were predicted. DDES results contain a harmonic at twice the BPF for thrust. This is not present for the finer grid of Jang and Mahesh (2013) LES results and VPWT results. DDES and experiment contain a higher harmonic at twice the BPF for side-force magnitude. LES does not resolve this frequency for side-force.

4.2 Propeller 7371R in Crashback, Introduction to Flow Regimes

Propeller 7371R produced common flow behaviors that were temporally consistent. Each behavior occurred for a wider range of advance coefficients than propeller 4381. This provided a unique opportunity to perform a broad classification of crashback operations. Each common flow behavior for different advance coefficients was grouped into a regime. Four flow regimes are identified in the third quadrant of the OWC in Figure 9 and the plot of resultant side-force in Figure 10 below. A transition case is also identified at $J = -1.0$ that exhibited behavior of multiple regimes. Propeller forces for 7371R in each regime showed consistent trends. Regime I covers low magnitude advance coefficients where propeller induced flow dominates the free-stream flow and moderate levels of thrust and torque are produced. Regime II flow behavior creates a minimum thrust and torque state due to high symmetry of the induced flow from the axisymmetric ring vortex present in the flow field. Both regime I and II contain lower levels of radial velocity and high symmetry
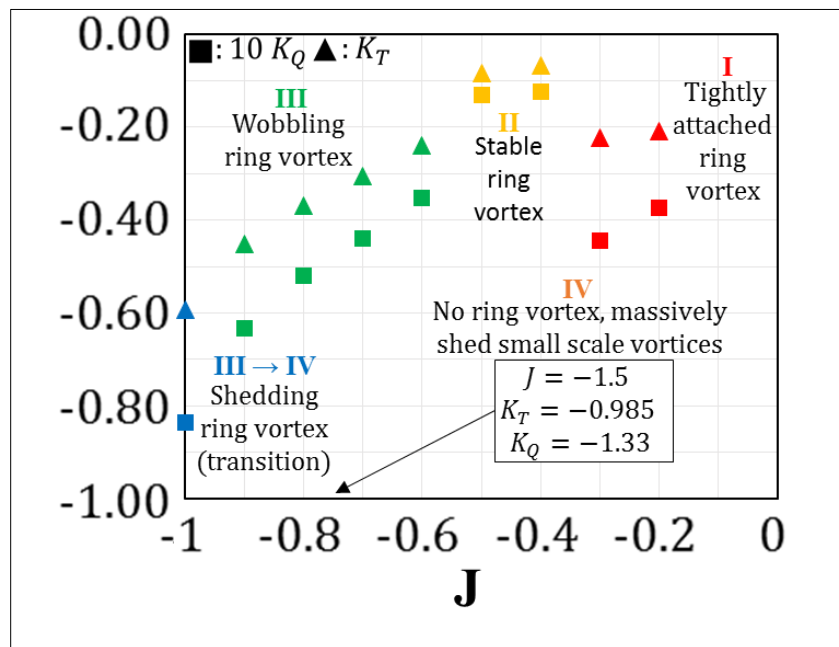
Figure 9: Results of OWC for 7371R in crashback with flow regime classifications. Points are labeled by their flow regime behavior.

28

resulting in low side-forces. In regime III ring vortex symmetry is broken leading to asymmetry in the induced flow. This causes thrust, torque and side-forces to increase with advance coefficient. At J = -1.0 behavior consistent with both regimes III and IV are seen, maintaining high values of thrust, torque and side-force. In regime IV, the flow behavior is broadly characterized as a massively separated wake, which increases axial drag with incoming flow velocity but does not significantly increase forces perpendicular to the axial direction.
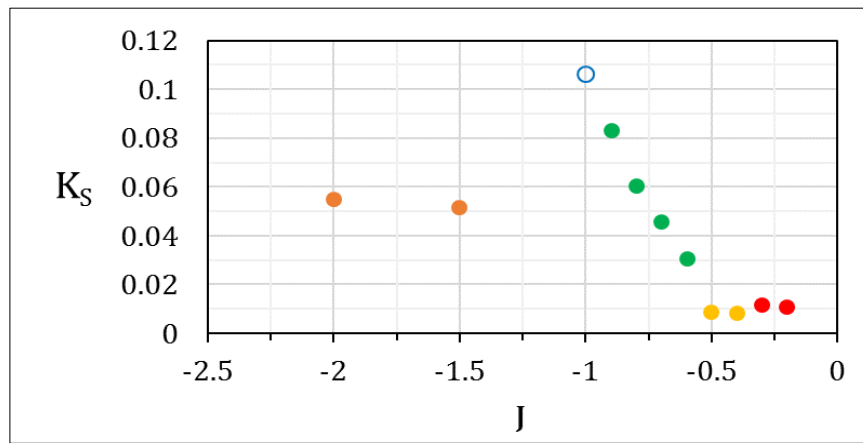
Figure 10: Resultant side-force coefficient (K_S) for 7371R in crashback labeled by flow regimes. Points are colored by there regime classification

The flow regimes will be introduced in greater detail in the following subsections. In-depth discussion of flow regime behavior and its effects on propeller forces and harmonics are discussed in detail in a later section. Some of the flow regimes identified for 7371R were also observed for 4381, therefore both geometries are discussed. However, the same flow regime is not always exhibited for a given magnitude of the forces for both propellers. The following discussion of flow regime behavior in 4.2 and also in 4.4 is for the medium grid only of both propellers. The fine grid for the grid study of 7371R will be discussed in section 4.4 on flow behavior.

www.manaraa.com

4.2.1 Flow regime I: tightly attached ring vortex on blade tips, secondary upstream jet circulation

For small magnitude advance coefficients before a sharp decrease in thrust and torque (see OWC in Figure 9), the flow is characterized by two areas of circulation. The primary area of circulation is located near the blade tips. This circulation is a result of the blade tip vorticity interacting with the obstructing flow from upstream. This produces a small, tightly attached ring vortex around the entire circumference of the propeller at the blade tips (opaque structures in Figure 11, area of large negative pressure in Figure 12). In this regime, the free-stream velocity is small with respect to the blade tip velocity therefore the momentum output from the propeller dominates the momentum of the incoming free-
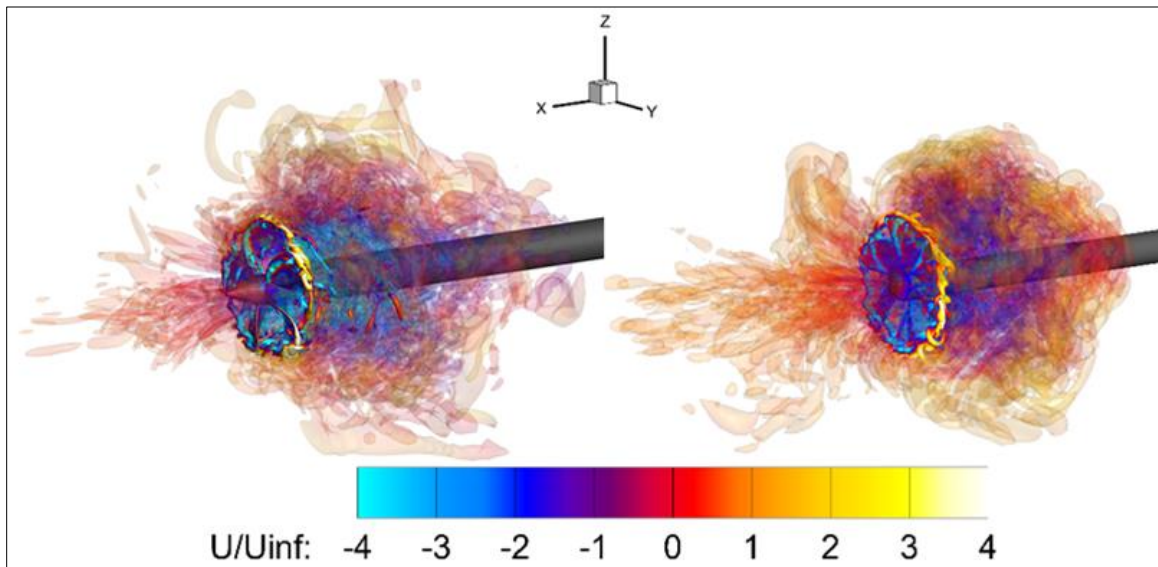
Figure 11: Instantaneous flow field of regime I for 7371R and 4381 at J = -0.3. 3D vortices shown. Vortex structures are resolved by isosurfaces of Q-Criterion colored by axial velocity, normalized by the free-stream velocity.

stream flow. The result is a turbulent jet that travels upstream from the propeller (translucent structures in Figure 11). The shear between the jet and the free-stream produces an area of secondary circulation upstream of the propeller (shown by streamlines in Figure 12 below). This is described by Mahmoudi and Fleck (2016) for a round wall jet in counterflow. The two areas of circulation are co-rotating. This creates a stable flow field

المنارة للاستشارات

www.manaraa.com

which, when phase averaged, shows strong axisymmetry around the propeller's axis of rotation. A phase average for $J = -0.3$ was taken using flow solutions for every $10°$ of propeller rotation for a total of 100 propeller rotations, shown in Figure 12. The velocity contour in Figure 12 has symmetry on the plane shown about the constant z-plane that goes through the propeller axis. On the right in Figure 12, although both propellers are operating at the same advance coefficient, the upstream secondary circulation is positioned closer to the propeller plane axially and further from the propeller plane radially for propeller 7371R. This is a result of propeller 7371R producing less thrust at the same advance coefficient,
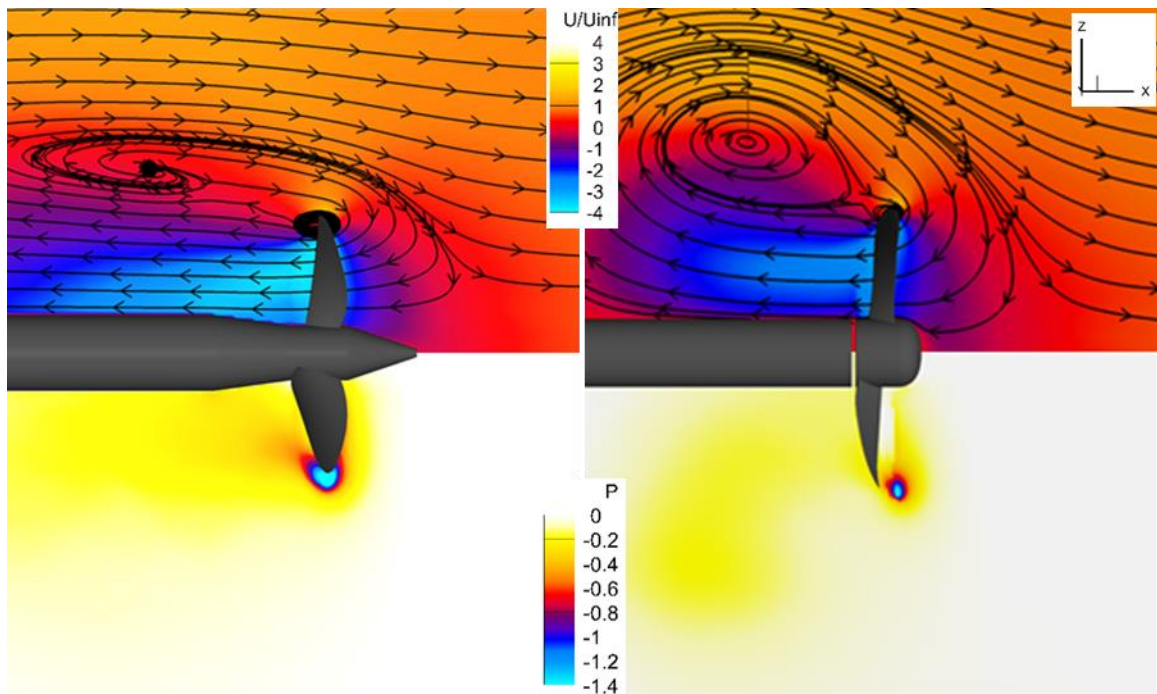
Figure 12: Average flow field of regime I for 7371R and 4381 at J = -0.3. Axial slice on propeller center plane with streamlines. 4381 (left) 7371R (right). Phase average was taken every 10° of rotation. Contour colored by axial velocity normalized by the free-stream velocity (top) and pressure contour non-dimensionalized by ρU_0^2 (bottom).

allowing the free-stream momentum to dominate the propeller produced momentum. Part of the propeller outflow is re-ingested after it circulates around the propeller disk and into the inflow plane. Large scale production and reingestion of turbulent structures in the blade passages and the blade tip vortices tightly attaching to the blade tips causes high

31

frequencies to dominate the time histories of thrust and horizontal side-force. Figure 13 contains the filtered time histories for thrust and horizontal side-force for flow regime I cases J = -0.2 and -0.3. Large fluctuations are present due to interaction with turbulent structures. No consistent low frequency presents itself in the time histories, but they are
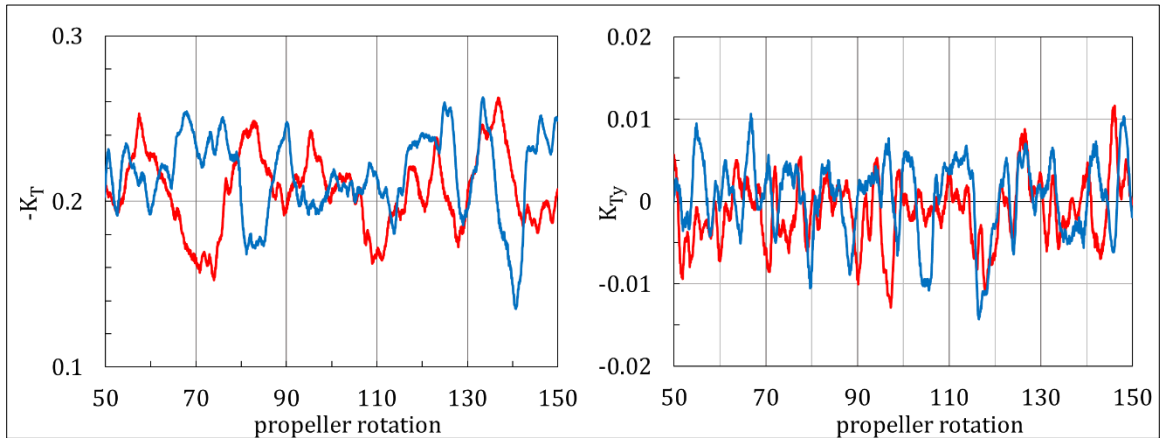
Figure 13: 7371R regime I time histories for thrust (K_T) and horizontal side-force (K_{Ty}) coefficient, J = -0.2, -0.3. J = -0.2 (red),-0.3 (blue). Time histories have been filtered to exclude frequencies higher than 1 propeller rotation.
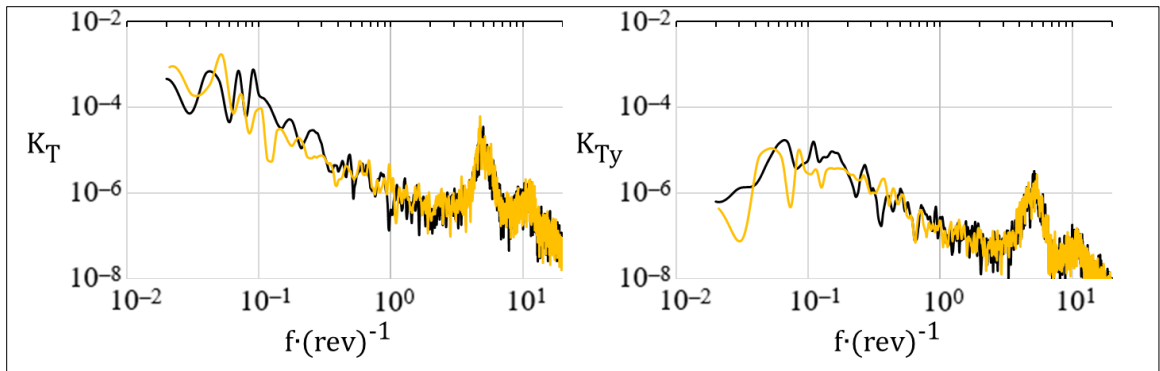
Figure 14: 7371R regime I PSDs for thrust (K_T) and horizontal side-force (K_{Ty}) coefficient, J = -0.2, -0.3. J = -0.2 (gold), J = -0.3 (black). Frequencies are normalized by propeller rotational speed.

present. This observation is reinforced by the PSDs for thrust and side-force in Figure 14. The clear dominant frequencies occur around BPF and twice BPF. It was expected that these frequencies would be very close to 6 blade passages. However, the two dominate frequencies that appear for regime I are lower than BPF for a 6 bladed propeller at 4.74 for thrust and 5.16 for side-force. Positive tangential velocities with respect to propeller

32

rotational direction and the lack of a large ring vortex circulation near the blade tips causes a shift in the frequencies.

4.2.2 Flow regime II: stable ring vortex behind propeller plane

As the free-stream momentum increases beyond that in regime I, the two areas of circulation combine to form a single circulation region near the propeller tips, just behind the propeller disc. This circulation takes the form of an axisymmetric ring vortex about the propeller's axis of rotation, shown in Figure 15 below. In front of the propeller, the free-stream momentum quickly dominates the thrust of the propeller causing the propeller induced flow to recirculate around the outside of the propeller disk towards the downstream side of the propeller. The uniform ingestion of the flow behind the propeller ensures stability of the ring vortex in its axisymmetric form.
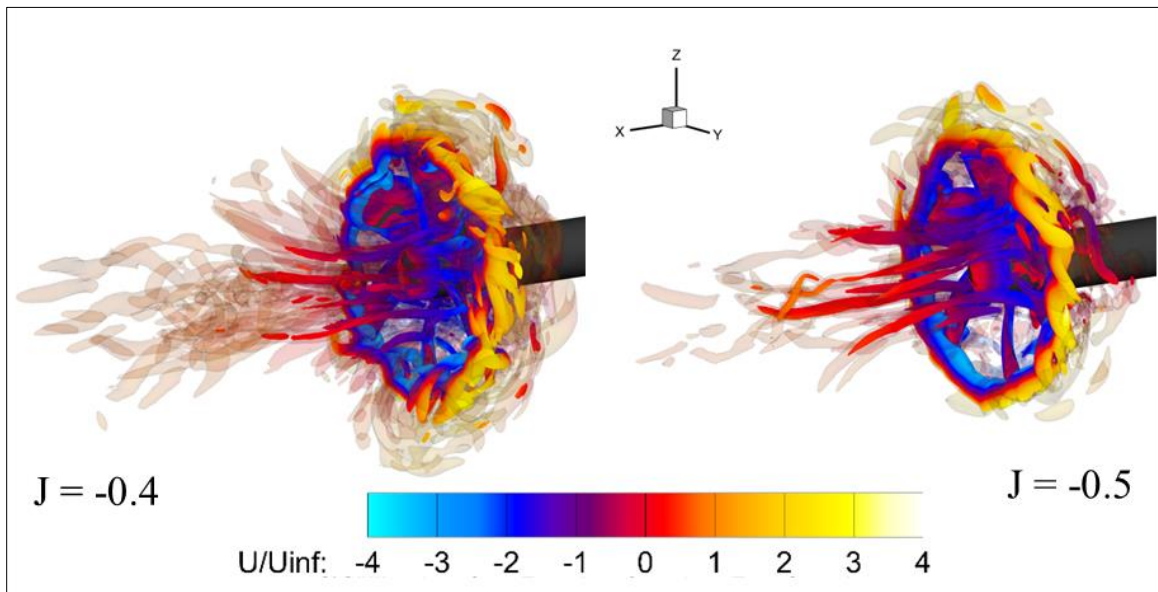
Figure 15: Instantaneous flow field of regime II for 7371R at J = -0.4, -0.5. 3D vortices shown. Vortex structures are resolved by isosurfaces of Q-Criterion colored by axial velocity, normalized by the free-stream velocity.

The phase average of the flow is strongly axisymmetric for this regime, shown in Figure 16 below. A 10° propeller rotational phase average was performed for a total of 100 propeller rotations. The ring vortex is pictured at its highly stable location, just behind the

leading edge (trailing edge in ahead operation) of the propeller blades. A secondary region of circulation appears in the mean flow upstream of the propeller as a separation along the surface of the shaft. This separation is a result of the stagnation point between the free-stream flow and propeller induced flow upstream moving axially closer to the propeller disk (from regime I to regime II). The higher levels of shear close to the propeller disk for J = -0.4 and -0.5 between the free-stream flow and propeller induced flow create a visible stagnating circulation region along the shaft.

This regime has been compared to vortex ring state (VRS) in rotorcraft. Ring vortex state occurs in the event of a steep angle of decent at a high rate of speed, relative to the ground, so that the there is a significant relative velocity between the rotor disk and
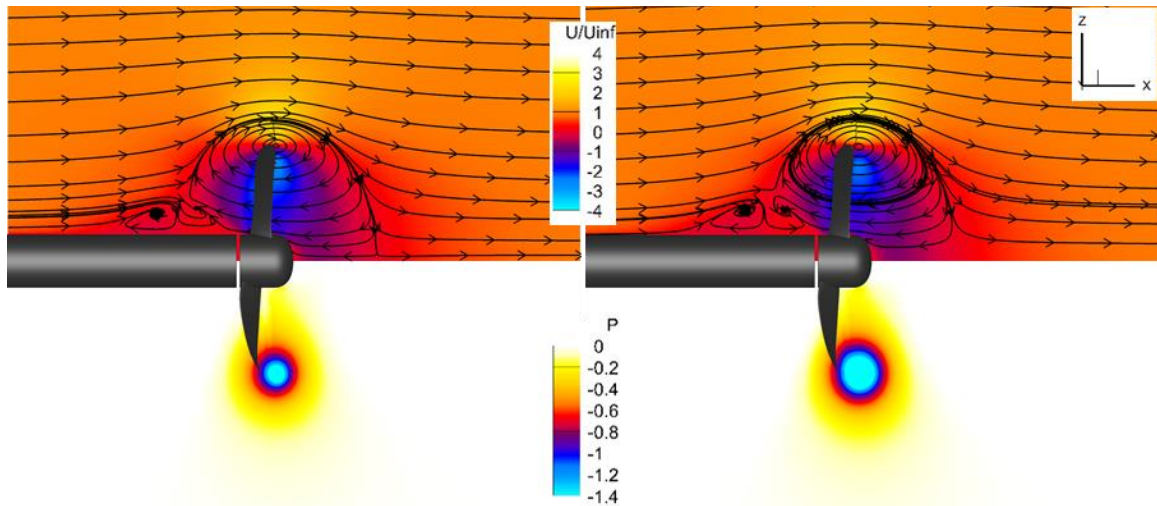
Figure 16: Average flow field of regime II for 7371R at J = -0.4, -0.5. Axial slice on propeller center plane with streamlines. 4381 (left) 7371R (right). Phase average was taken every 10° of rotation. Contour colored by axial velocity normalized by the free-stream velocity (top) and pressure contour non-dimensionalized by ρU_0^2 (bottom).

the air coming into the disk from the descent maneuver. This relative velocity behaves similar to the free-stream velocity in Figure 16, causing the rotor to ingest its own wake. This creates a ring vortex that persists at the tip of the rotor blades until the relative inflow

34

velocity is changed to destroy this self-ingesting state. Details of VRS can be found in Green et al. (2005) and Johnson (2005).

As a result of this self-ingesting axisymmetric state, propeller forces are at a minimum in regime II. Figure 17 contains the time histories of thrust and side-force for 7371R regime II cases. The time histories have been filtered as was done for regime I time histories, where any higher frequency than one propeller rotation has been filtered out of the signal. The force time histories of regime II cases are dominated by higher frequencies
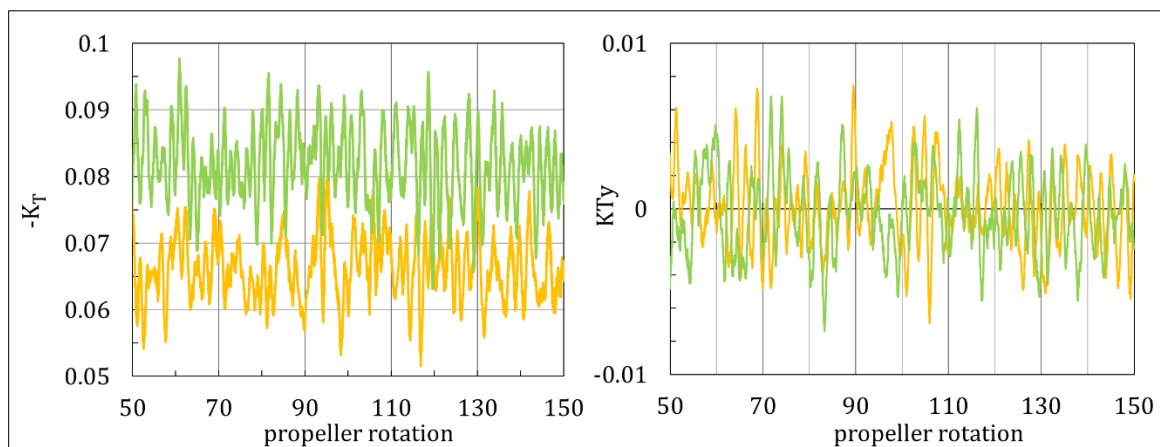
Figure 17: 7371R regime II time histories for thrust (K_T) and horizontal side-force (K_{Ty}) coefficient, J = -0.4, -0.5. J = -0.4 (gold), -0.5 (green). Time histories have been filtered to exclude frequencies higher than 1 propeller rotation.

more than those in regime I (see Figure 13). Mean thrust values are 60% to 70% less than those in regime I, and the amplitude of thrust fluctuations are 80-85% smaller than the lower frequency fluctuations of regime I cases. Side-force amplitudes are comparable (see Figure 10), but regime II fluctuations are less energetic. Mean thrust values for regime II cases do not compare as well as the two regime I cases. J = -0.5 produces about 22.7% more thrust than J = -0.4. J = -0.3 produces only 7.3% more thrust than J = -0.2. Looking at the right-hand side of Figure 16, it is obvious that the vortex is stronger for J = -0.5.

Figure 18 shows the PSDs for thrust and horizontal side-force. Comparing to the PSDs of regime I cases, it confirms the lack of low frequency content of the forces, as there

35

is a steep drop in energy for frequencies lower than one propeller rotation. A more defined

peak is resolved near BPF and twice BPF. The dominate frequencies are closer to BPF and

twice BPF than regime I cases at about 5.8 and 11.3 cycles per propeller rotation. The shift

in dominate frequency phase towards multiples of BPF is attributed to an increase in axial

velocity at propeller inflow. Thus the fluctuating flow through the blades interacts with the

next blade passage more frequently than in regime I.
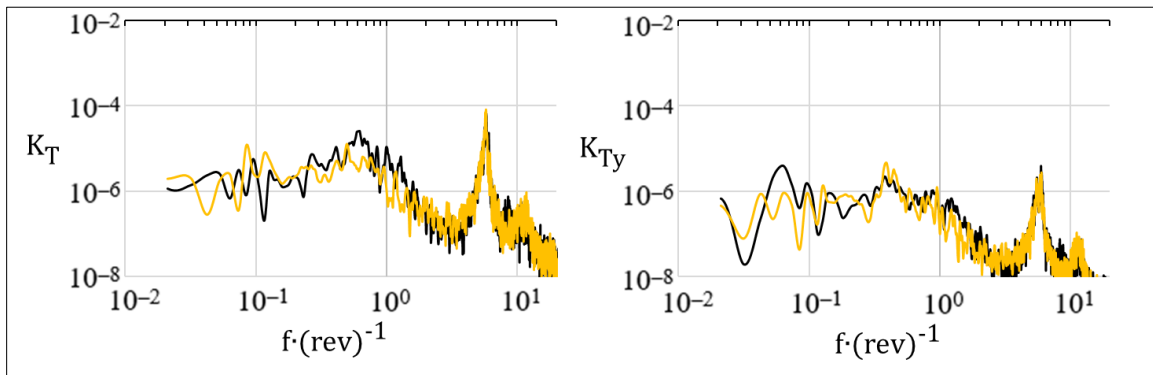
Figure 18: 7371R regime II PSDs for thrust (K_T) and horizontal side-force (K_{Ty}) coefficient, J = -0.4, -0.5. J = -0.4 (gold), J = -0.5 (black). Frequencies are normalized by propeller rotational speed.

It is worth noting at this point in the progression of flow regimes, 7371R has reached

its minimum thrust point. However, for 4381 J = -0.5 is in its minimum thrust region, but

the flow behavior is still in regime I. This is shown in Figure 19 below. Two areas of

circulation persist, as was seen for regime I for 7371R geometry. The secondary upstream

circulation is very close axially and radially to the propeller disk indicating that this

operation point is near the transition to regime II. Despite this similarity in state before the

transition to regime II, it is unknown if this geometry is capable of producing a stable

regime II state. The next operating point simulated was J = -0.6, which is shown in the next

section to produce regime III behavior. This implies that a stable regime II state of 4381

must exist at an advance coefficient between J = -0.5 and -0.6. This is a very narrow range

of operation, indicating regime II behavior is very unstable, regarding flow behavior

quickly shifting from regime I to regime III from J = -0.5 to -0.6. Chang et al. (2008) characterized the dominant flow behavior at J = - 0.5 for 4381 as a ring vortex around the
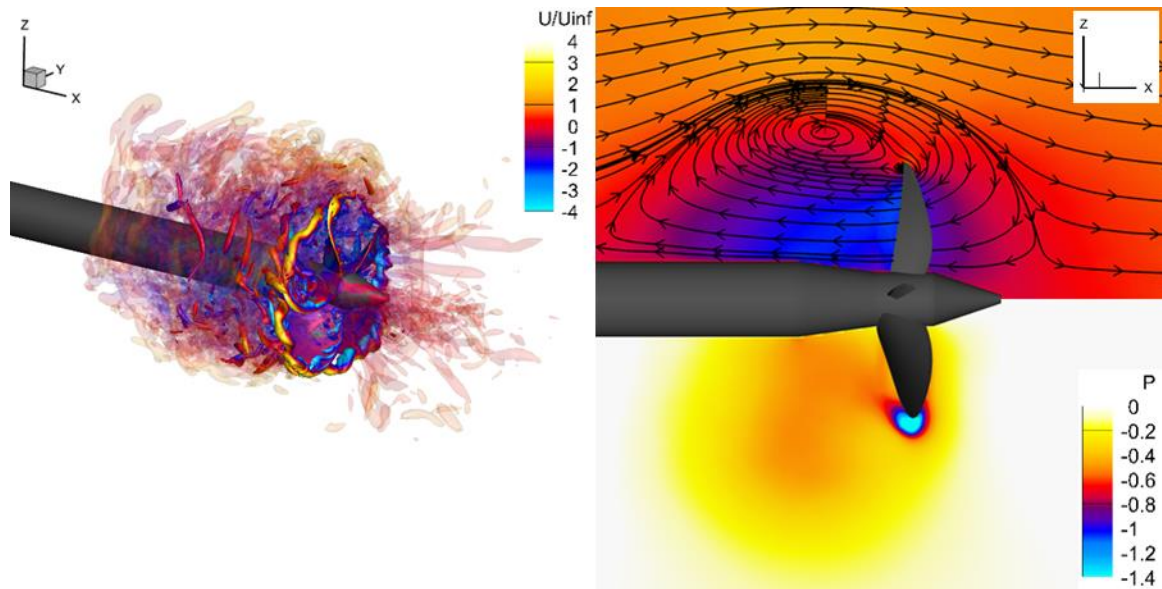
Figure 19: 4381 (still in) regime I instantaneous &average flow field, J = -0.5. 3D vortices and axial slice on propeller center plane with streamlines shown. Vortex structures are resolved by isosurfaces of Q-Criterion colored by axial velocity, normalized by the free-stream velocity (left). Phase average was taken every 10° of rotation (right). Contour colored by axial velocity normalized by the free-stream velocity (top) and pressure contour non-dimensionalized by ρU_0^2 (bottom).

propeller blades as in regime II for propeller 7371R. Chang et al. (2008) observed this jet behavior in Figure 19 for J = -0.5, but only for infrequent high amplitude thrust events in the time history, resulting from a breakdown in the axisymmetric ring vortex into an upstream jet state. This bi-modal behavior between regimes I and II is not observed for 7371R or 4381 DDES results. However, more simulation time would be required for 4381 to improve certainty in this observation.

4.2.3 Flow regime III: wobbling stable ring vortex

An instability forms in the stable ring vortex in regime II resulting in asymmetry of the ring vortex shape. A section of the ring vortex is attached to multiple blades, pictured in Figure 20 below. The ring vortex is attached to three blades near their tips, shown as blade 1, 2, 5 for 4381 and 1, 2, 6 for 7371R. Attachment to blade 5 for 7371R is intermittent.

The remainder of the ring vortex is stretched away from the blade tips. This section is deformed axially and radially so that there is a tilt of the ring vortex in relation to the propeller plane. Blades 3 and 4 for 4381 and 7371R cannot interact with the ring vortex due to this deformation. Reattachment to the blade tip region of the ring vortex resides near the area of blade 2 in Figure 20. This reattachment causes a kink in the ring vortex as the ring vortex core rapidly turns and reattaches to the stable region near the blade tips.
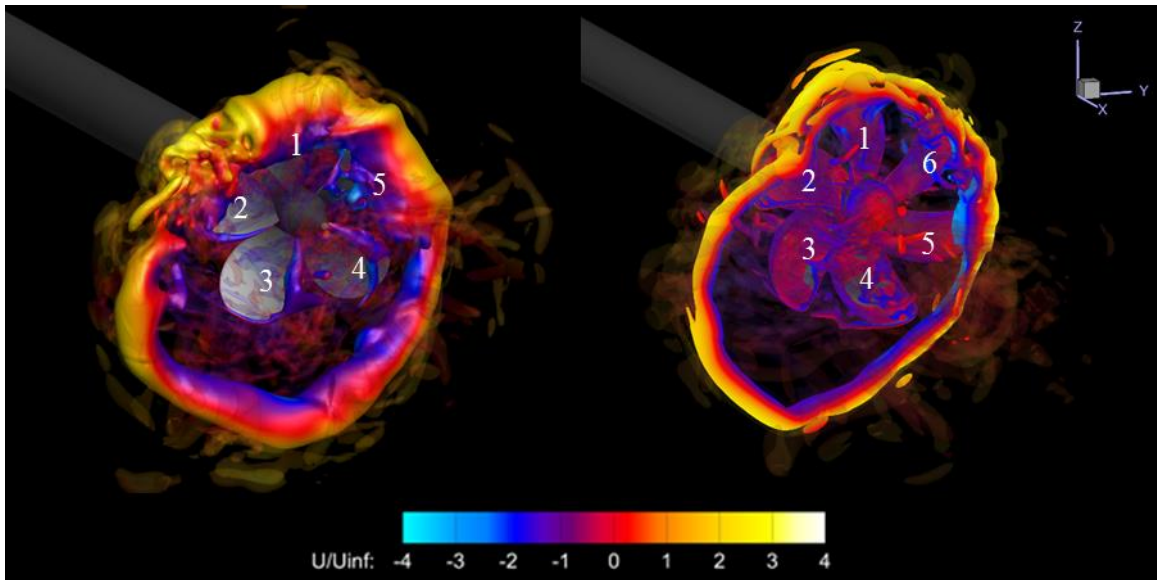
Figure 20: Instantaneous flow field of regime III for 7371R and 4381 at J = -0.7. 3D vortices shown. Vortex structures are resolved by isosurfaces of Q-Criterion colored by axial velocity, normalized by the free-stream velocity.

A phase average of this flow regime is shown in Figure 21 below. The average was taken every 10° of rotation for an integer number of ring vortex rotations. The plane shown is a constant y-plane along the centerline of the propeller hub and shaft. Comparing the flow field to regime II, it is shown that the upstream separation is lost in the average, and the center of rotation of the main ring vortex has moved axially downstream of the blade tips. It should be noted that the asymmetry of the ring vortex shape causes some smearing in the average flow solution. The symmetry about the z-plane at the centerline of the propeller shaft is preserved in the average by including an integer number of ring vortex

38

rotations. The area in which the stretched section of the ring vortex wanders is shown in the pressure field (bottom Figure 21) as the area of moderate negative pressure (red and orange regions). The center of the attached section of the ring vortex is marked where negative pressure magnitude is highest.
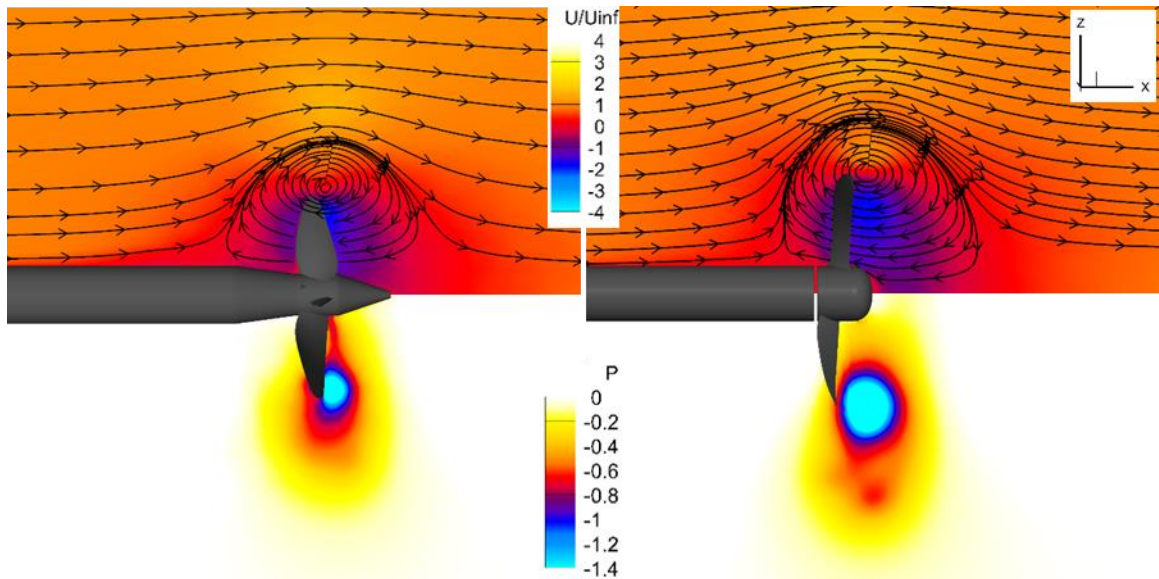
Figure 21: Average flow field of regime III for 7371R and 4381 at J = -0.7. Axial slice on propeller center plane with streamlines. 4381 (left) 7371R (right). Phase average was taken every 10° of rotation. Contour colored by axial velocity normalized by the free-stream velocity (top) and pressure contour non-dimensionalized by ρU_0^2 (bottom).

For all advance coefficients in this regime, the ring vortex rotates opposite to the direction of propeller rotation. This is shown in Figure 22 for two-thirds of a ring vortex rotation cycle for both 4381 and 7371R at J = -0.7. The view shown has the propellers rotating counter-clockwise in reverse operation while the ring vortex is pictured rotating clockwise. Propeller 7371R produces a highly stable wobbling rotating ring vortex for regime III cases of J = -0.6 → -0.9. Propeller 4381 does not exhibit the same level of stability for such a wide range of advance coefficients. A breakdown of ring vortex regime III behavior into regime II behavior is shown in Figure 23. This observation of 4381

39
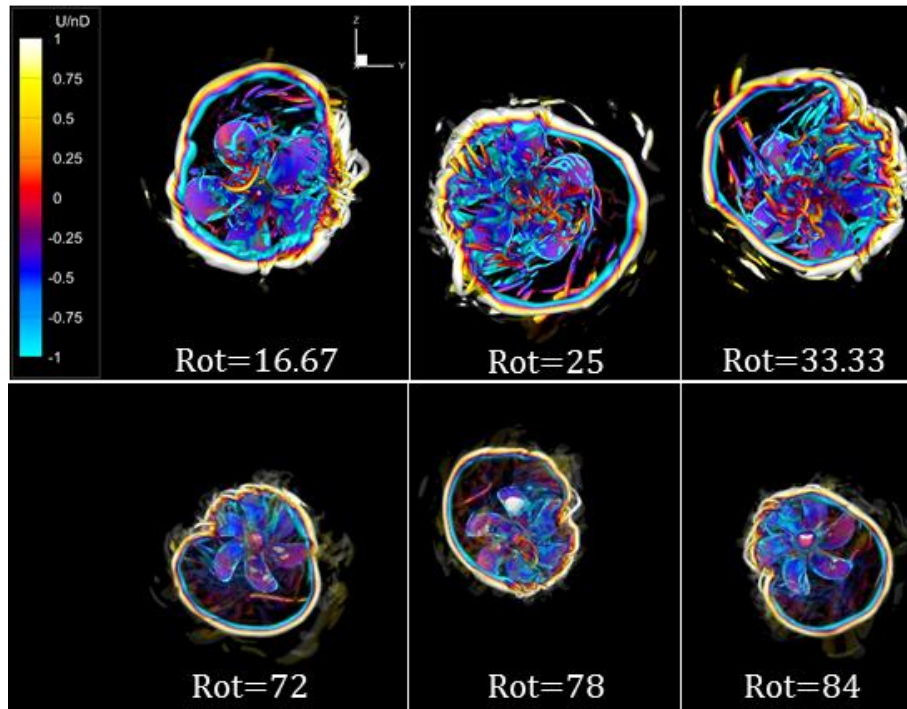
Figure 22: Frames showing rotation of wobbling ring vortex in regime III. 4381 (top) and 7371R (bottom). Vortex structures are resolved by isosurfaces of Q-Criterion colored by axial velocity, non-dimensionalized by nD.
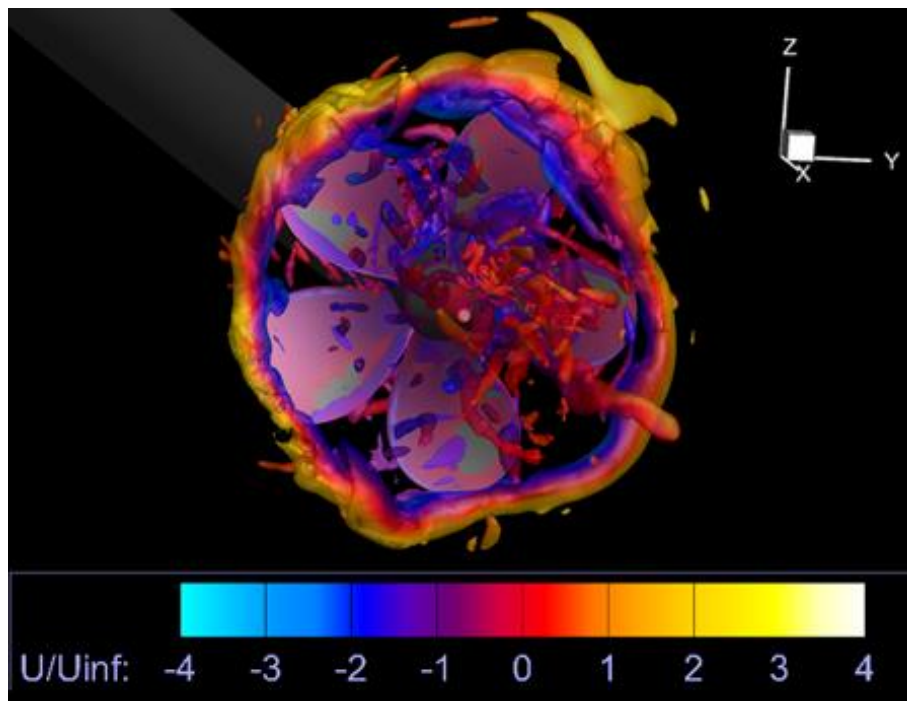
Figure 23: Low thrust event for 4381 in crashback at J = -0.7.Instantaneous flow field. 3D vortices shown.Vortex structures are resolved by isosurfaces of Q-Criterion colored by axial velocity, normalized by the free-stream velocity.

40

requires more simulation time to investigate effects of pressure convergence and grid refinement on the repetition of these events.

As a result of the ring vortex asymmetry and the ring vortex rotating opposite to the propeller rotational direction, a clear low frequency first harmonic is formed in the side-forces and a shift in multiples of BPF occur for regime III cases. The first harmonic of side-forces is clearly visible in Figure 24 below. The side-force's first harmonic frequency changes with advance coefficient. A higher order instability forms causing a first harmonic to develop in thrust as advance coefficient increases. This first harmonic is not present for J = -0.6, begins to develop for J = -0.7 and is well defined for J = -0.8 and -0.9.

Figure 24: 7371R regime III time histories for thrust (K_T) and horizontal side-force (K_{Ty}) coefficient, J = -0.6, -0.7, -0.8, -0.9. Time histories have been filtered to exclude frequencies higher than 1 propeller rotation.

The frequencies for each case in regime III are presented in Figure 25 below. The first harmonic for thrust is shown for J = -0.8 and -0.9 on the left. The cause of this first harmonic will be discussed in a later section. Although there seems to be a first harmonic forming for J = -0.7, it is not persistent in the time history and thus is not clear in the PSD for that case. However, it will be shown later that for J = -0.7 a finer grid of 7371R will produce a steadier first harmonic in thrust that is more readily apparent when viewing its

41

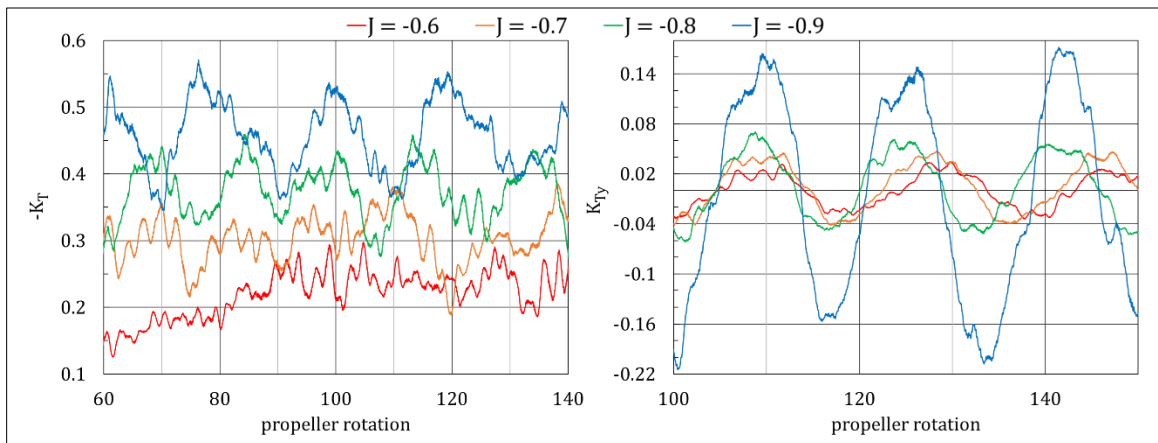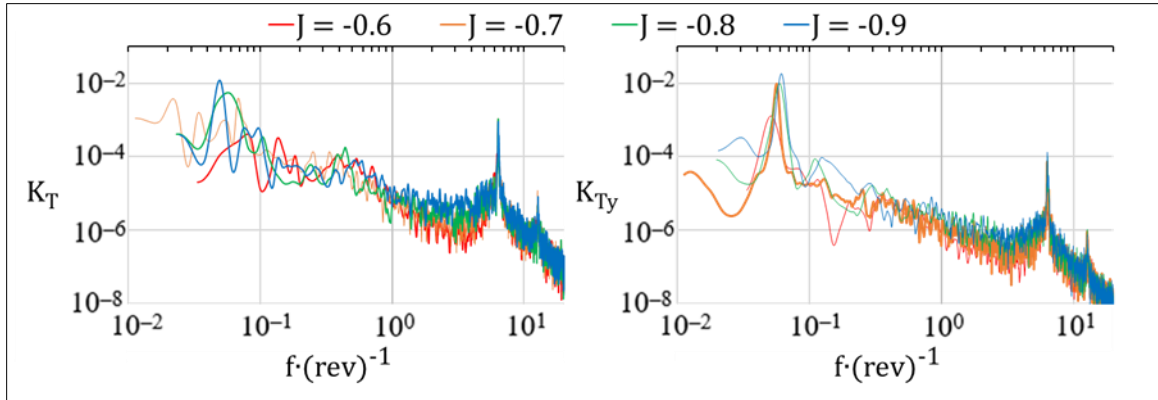**Figure 25: 7371R regime III PSDs for thrust (K_T) and horizontal side-force (K_{Ty}) coefficient, J = -0.6, -0.7, -0.8, -0.9. Frequencies are normalized by propeller rotational speed.**

time history and PSDs. The progression of the first harmonic in side-force is shown on the right in Figure 25. There is a relatively large increase in frequency and amplitude from J = -0.6 to -0.7, subsequently this increase in frequency and amplitude begins to level off. The dominate high frequencies are slightly greater than BPF and twice BPF at about 6.3 and 12.6 cycles per revolution, respectively. This is expected because of the opposite rotation of the ring vortex with respect to propeller rotation increasing the frequency of blade passage interactions.

4.2.4 Flow regime III→IV: shedding wobbling ring vortex (transition)

As the free-stream momentum increases beyond that in regime III, the wobbling ring vortex is destabilized and it begins to shed. Figure 26 shows an instantaneous solution and the average solution for J = -1.0 for 7371R. The instantaneous solution on the left shows the initial breakdown of the ring vortex. This breakdown occurs on the section of the ring vortex stretched away from the blade tips, with the shedding cascading circumferentially into other sections of the ring vortex. The phase averaged solution was taken every 10º of rotation for the time history of the simulation where the ring vortex was fully-developed and had not shed (right Figure 26). Comparing to the average solution of regime III, the location of the ring vortex has moved axially away from the blade tips in

42
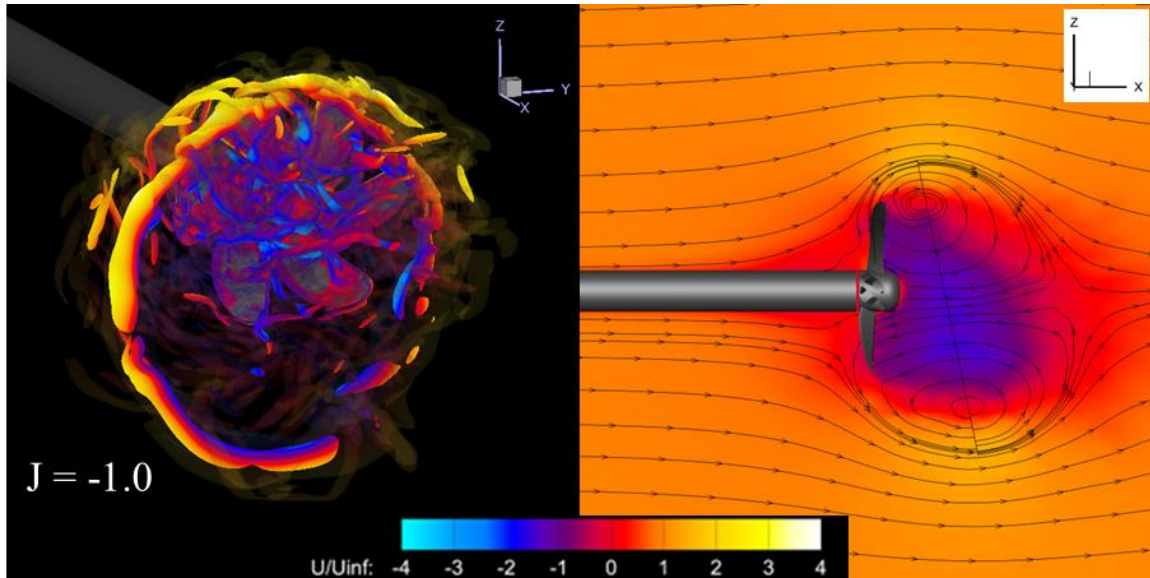
Figure 26: 7371R transition case from regime III→IV, J = -1.0. 3D vortices and axial slice on propeller center plane with streamlines shown. Vortex structures are resolved by isosurfaces of Q-Criterion (left). Phase average was taken every 10° of rotation (right). Both contours colored by axial velocity normalized by the free-stream velocity.

the section of the ring vortex attached to the blades. Larger axial and radial wandering with respect to regime III cases is shown in the section of the ring vortex adjacent to the attached section. The outflow of the propeller into the incoming free-stream flow is noticeably inhibited, shown by the streamlines being deflected radially much sooner than in regime III. The higher momentum inside of the free-stream increases the area of influence of the circulation created by the ingestion of the propeller downstream reaching much farther radially and axially than in regime III. The combination of the free-stream obstructing the blade passage flow and the increased size of the area of influence destabilizes the ring vortex and causes it to shed.

Figure 27 contains the time histories for thrust and horizontal side-force coefficient of this transition case. The minimums in thrust are marked by the gold dots in Figure 27. The decrease in thrust before these points corresponds to a contraction of an asymmetric ring vortex state towards a more axisymmetric ring vortex near the propeller blade tips.
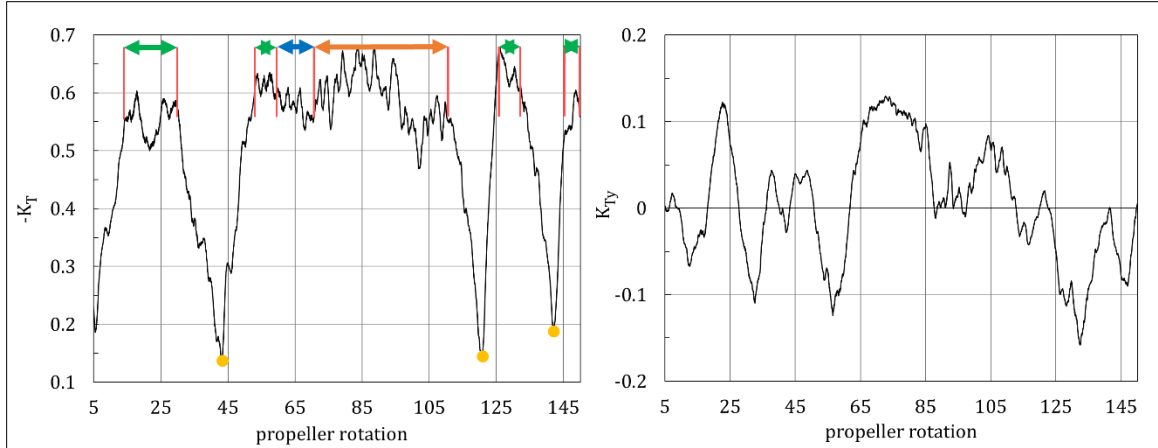
Figure 27: 7371R transition case from regime III→IV, J = -1.0. Time histories for thrust (K_T) and horizontal side-force (K_{Ty}) coefficient. Multiple regime behaviors labeled. Time histories have been filtered to exclude frequencies higher than 1 propeller rotation. Regime III behavior marked by green intervals, regime II states by gold points, vortex breakdown by blue interval and regime IV behavior by orange interval.

An instantaneous solution for each minimum state is shown in Figure 28. Note that the first minimum is closest to a regime II state and thus its thrust magnitude is the smallest compared to the other two minimum states. At the second minimum point the ring vortex is stretched along a section of its circumference corresponding to an increase in thrust. Since the ring vortex at the third minimum point is stretched farther it has a greater thrust magnitude than the second minimum point. This mechanism for increased thrust will be discussed in greater detail in a later section for regime III.
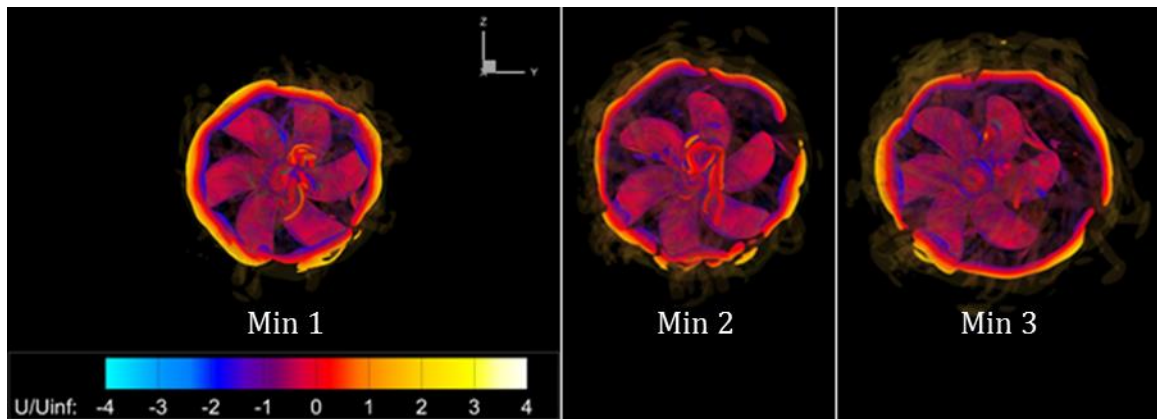
Figure 28: 7371R transition case from regime III→IV, J = -1.0. Instances of minimum thrust, bimodal behavior from regime III→II Vortex structures are resolved by isosurfaces of Q-Criterion colored by axial velocity, normalized by the free-stream velocity.

44

www.manaraa.com

Vortex breakdown occurs in the blue interval marked in Figure 27. This is shown on the left-hand side of Figure 26. The orange interval corresponds to regime IV behavior. Details of this regime are provided in the next section. It is unclear whether this operating condition will repeat a transition to regime IV since the last part of the time history only includes transitions from regime II to III; continued simulation is necessary to confirm this behavior.

4.2.5 Flow regime IV: massively separated propeller wake

As free-stream momentum increases further, it begins to dominate propeller thrust output. Incoming free-stream flow can penetrate the blade passage flow and inflow induced by propeller ingestion on the downstream side is small with respect to the outer free-stream flow. Consequently, a ring vortex is unable to form, and massive shedding of the turbulent structures produced by the propeller blades occurs. This is shown on the left in Figure 29 as a wake of turbulent structures. The phase average wake is shown on the right in Figure 29 by streamlines and pressure contour of the $10°$ propeller phase average. The circulation of the wake is captured in the phase average but there is no distinct ring vortex present in the instantaneous flow. The streamlines also show the free-stream dominating the propeller output, creating a lack of outflow that extends significantly upstream from the propeller (as compared to regime III in Figure 21). This wake produces a massive low pressure region behind the propeller which causes a large negative thrust.

45
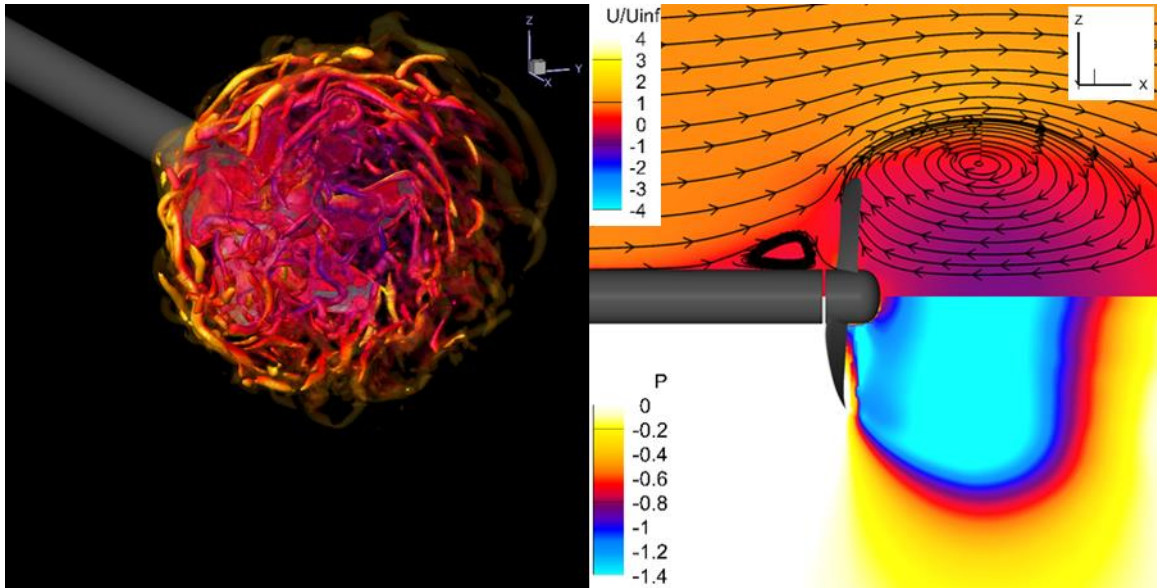
Figure 29: 7371R regime IV instantaneous &average flow field, J = -1.5. 3D vortices and axial slice on propeller center plane with streamlines shown. Vortex structures are resolved by isosurfaces of Q-Criterion colored by axial velocity, normalized by the free-stream velocity (left). Phase average was taken every 10˚ of rotation (right). Contour colored by axial velocity normalized by the free-stream velocity (top) and pressure contour non-dimensionalized by ρU_θ^2 (bottom).

The high levels of negative thrust are shown in Figure 30, which continually increases in magnitude with increasingly negative advance coefficient. The time history of the forces are dominated by random high frequencies, but lower frequency components appear for J = -1.5 compared to J = -2.0. The PSDs for regime IV cases contain no distinct dominate frequencies (Figure 31). There appears to be some concentration of energy near BPF, but these are not well-defined peaks as was seen in other regimes. In agreement with the time history, J = -2.0 is more energetic, especially at higher frequencies.

46

Figure 30: 7371R regime IV time histories for thrust (K_T) and horizontal side-force (K_Ty) coefficient, J = -1.5, -2.0. J = -1.5 (gold) and J = -2.0 (black). Time histories have been filtered to exclude frequencies higher than 1 propeller rotation.

Figure 31: 7371R regime IV PSDs for thrust (K_T) and horizontal side-force (K_Ty) coefficient, J = -1.5, -2.0. J = -1.5 (gold), J = -2.0 (black). Frequencies are normalized by propeller rotational speed.

47

4.3 Grid study for 7371R, Regime III at J = -0.7

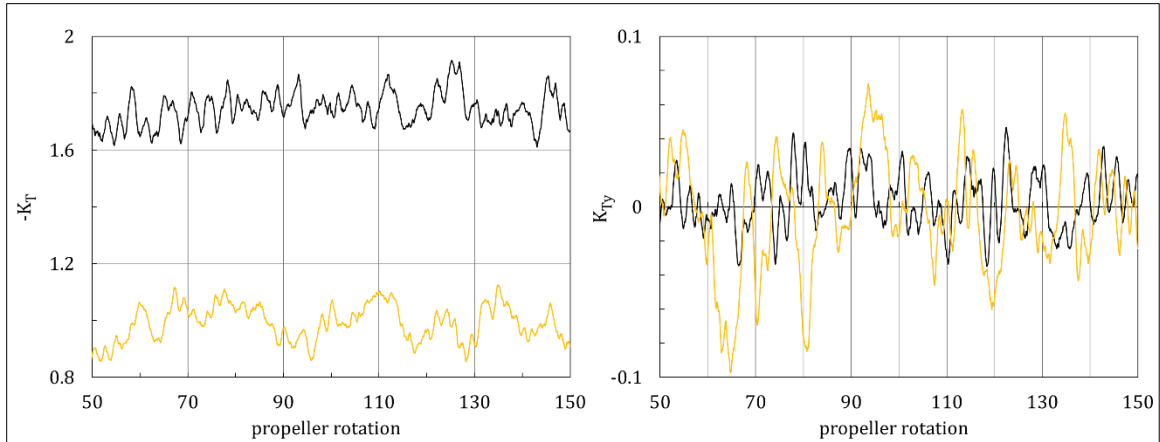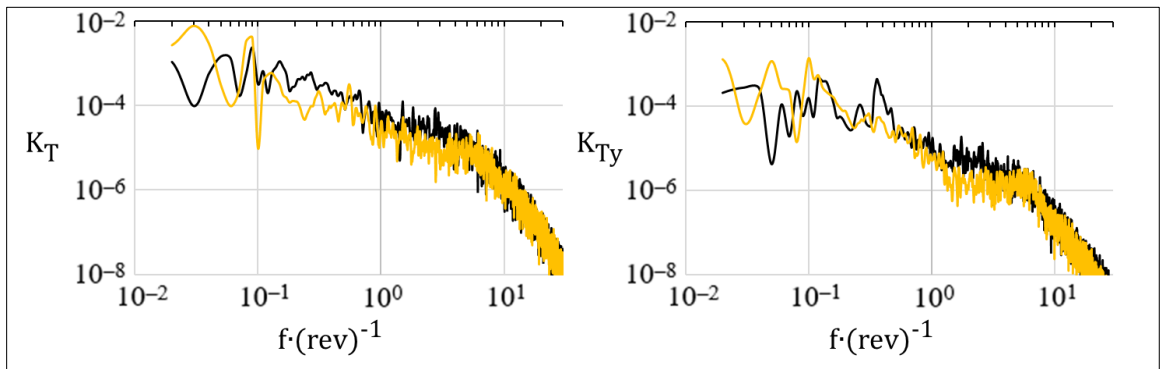The stability of the obtained flow solutions for 7371R regime III (see Figure 20) with respect to grid discretization was analyzed for the J = -0.7 case. This regime was chosen because of its unstable nature. A coarse, medium and fine grid system (details in Table 1) were simulated with the same flow conditions and time step. Average thrust, torque and resultant side-force coefficient values are compared in Table 3. Averages were taken for an integer number of ring vortex rotational periods of at least 6 periods. Fluctuations of the averages are represented by the root-mean square (RMS) values at the bottom of Table 3. Averages for thrust and torque show strong agreement for all grids when standard deviations are considered. Resultant side-force fluctuations are nearly equivalent between grids. Fluctuations of thrust are reasonably similar. Average torque values show a larger deviation between grids than thrust and side-force magnitude, but RMS fluctuations for torque are comparable.

Table 3: Grid study for 7371R J = -0.7. Comparison of thrust, torque and side-force coefficients

	Coarse	Medium	Fine
K_T	-0.3105	-0.2972	-0.3299
$10K_Q$	-0.4357	-0.4263	-0.4684
K_s	0.0445	0.0427	0.0426
$K_{T,rms}$	0.0483	0.0547	0.0578
$10K_{Q,rms}$	0.0737	0.0813	0.0859
$K_{s,rms}$	0.0142	0.0147	0.0167

Figure 32 shows the PSDs for thrust and horizontal side-force for all grids. The energy content for both thrust and side-force match well. Both thrust and side-force PSDs coincide for all grids at the BPF and twice BPF. Additionally, the first harmonic for side-force is in close agreement between all cases. This is shown on the right in Figure 33, which contains the time histories of the horizontal side-force for each grid, shifted so that they

48

overlap for at least one period. In general, the time histories and PSDs for each level of grid refinement demonstrate close similarity in the resolved behavior of the flow field for this operating condition. However, the fine grid PSD for thrust appears to have a present but inconsistent, first harmonic. This varying first harmonic is visible in the time history of thrust on the left in Figure 33. However, the more consistent first harmonic for the fine grid does not persist like J = -0.8 or -0.9 for the medium grid. The source of this first harmonic is discussed in detail in a later section for medium grid regime III advance coefficients.

Figure 32: 7371R grid study PSDs for thrust (K_T) and horizontal side-force (K_{Ty}) coefficient, J = -0.7. Coarse (gold), medium (black), fine (red). Frequencies are normalized by propeller rotational speed.
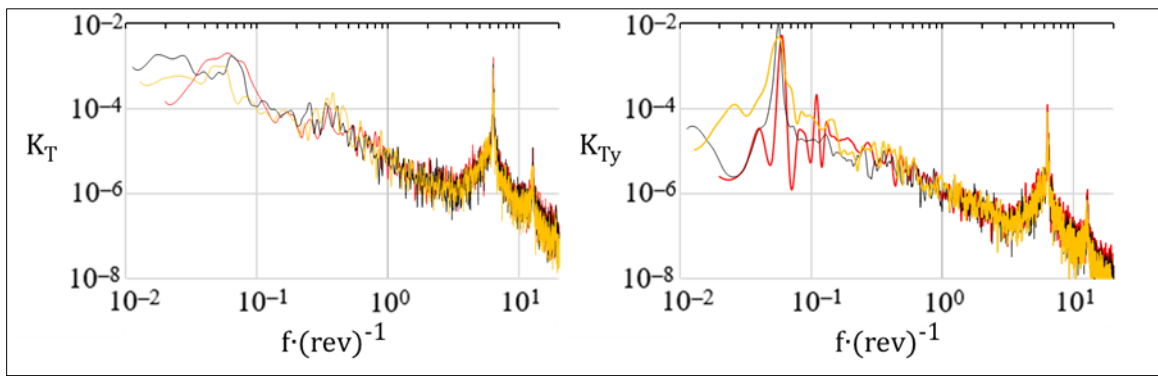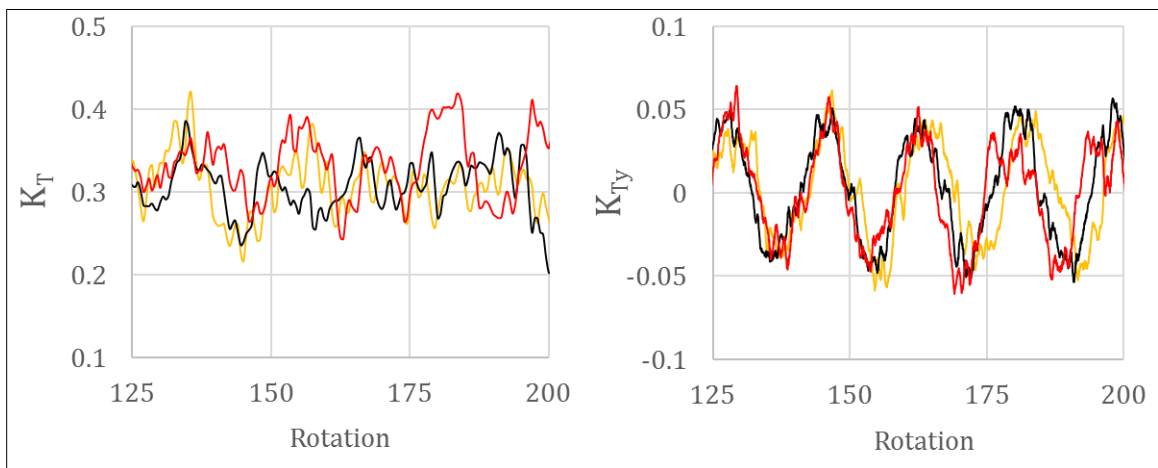

Figure 33: 7371R grid study time histories for thrust (K_T) and horizontal side-force (K_{Ty}) coefficient, J = -0.7. Coarse (gold), medium (black), fine (red). Time histories have been filtered to exclude frequencies higher than 1 propeller rotation.

49

4.4 Discussion of Flow Regimes

4.4.1 Regime I→II, transition from moderate to minimum thrust

As the advance coefficient increases in magnitude from regime I to regime II, thrust magnitude decreases significantly to a minimum for 7371R. Figure 34 shows the time histories for thrust coefficient for regime I and regime II cases. The signals have been filtered to remove high frequency fluctuations greater than one propeller rotation. The time signals show that thrust is similar between cases for a given regime, and thrust decreases between regime I and regime II by more than 50%. To track the decrease in thrust, despite the increase in free-stream momentum, 1D
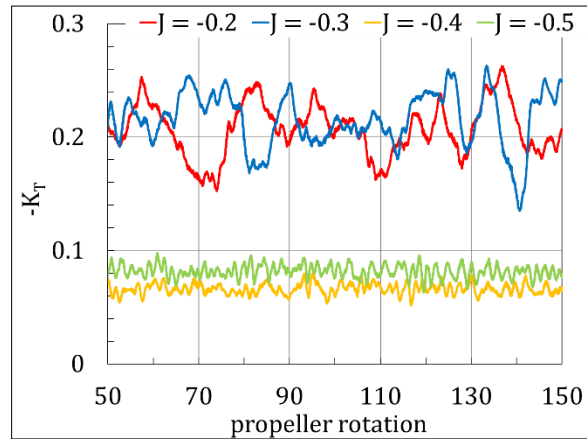
Figure 34: Time histories of thrust coefficient for regime I and regime II cases for 7371R.Time histories have been filtered to exclude frequencies higher than 1 propeller rotation.

radial distributions were created at the inflow plane. The increased momentum into the propeller is displayed in Figure 35 by the inflow axial velocity distributions. Figure 35 shows non-dimensional velocity, non-dimensionalized by velocity scale nD which is constant for all cases of 7371R. Inflow velocity of regime I cases are nearly identical whereas inflow velocity for regime II cases differ significantly and yet produce nearly the same thrust. A phase average taken every one propeller rotation for 7371R. The blade surface pressures on the pressure and suction side of the phase averages are shown in Figures 36 and 37, respectively. Regime I blade pressure distributions are very similar, but blade tip loading is higher on the suction side and the distribution on the pressure side is more positive for J = -0.3 resulting in an overall higher level of thrust for J = -0.3. Regime

50
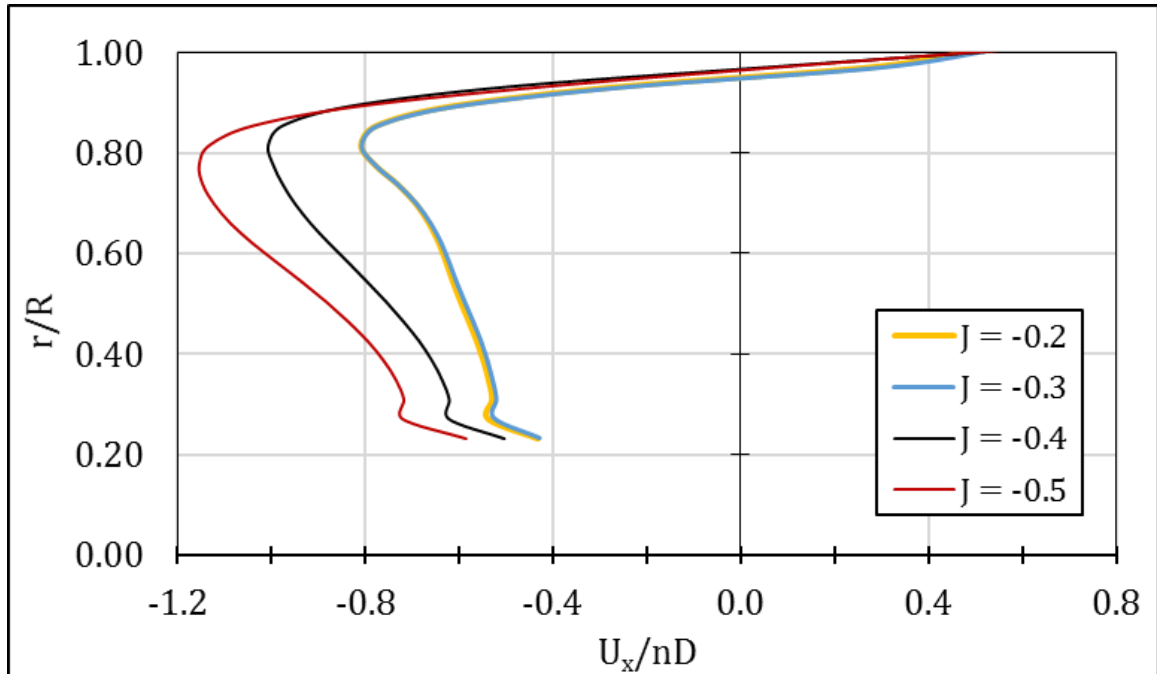
Figure 35: 1D radial distribution for axial velocity on inflow plane for regime I and regime II cases. Axial velocity non-dimensionalized by nD.

II blade pressure distributions are also very similar. However, J = -0.4 produces almost the same amount of thrust from smaller inflow velocity. This can be attributed to higher blade tip loading on the suction side and the relatively higher pressures near the bottom half of the leading edge (trailing edge in ahead) on the pressure side.

From regime I to II both the pressure and suction side distributions show more favorable values for thrust production for regime I cases. Much higher blade tip loading occurs for regime I cases on both the pressure and suction side. Overall, pressure distributions on the pressure side are significantly more positive for regime I compared to regime II. Very large positive pressure gradients occur near the leading edge, with pressure recovery occurring toward the trailing edge of the blade. This difference in pressure distributions can be attributed to the higher angles of attack of the incoming flow and the massive separations that occur for regime I cases. Flow separations are displayed by the deflection of the streamlines for regime I cases in Figures 36 and 37. Streamlines for

51
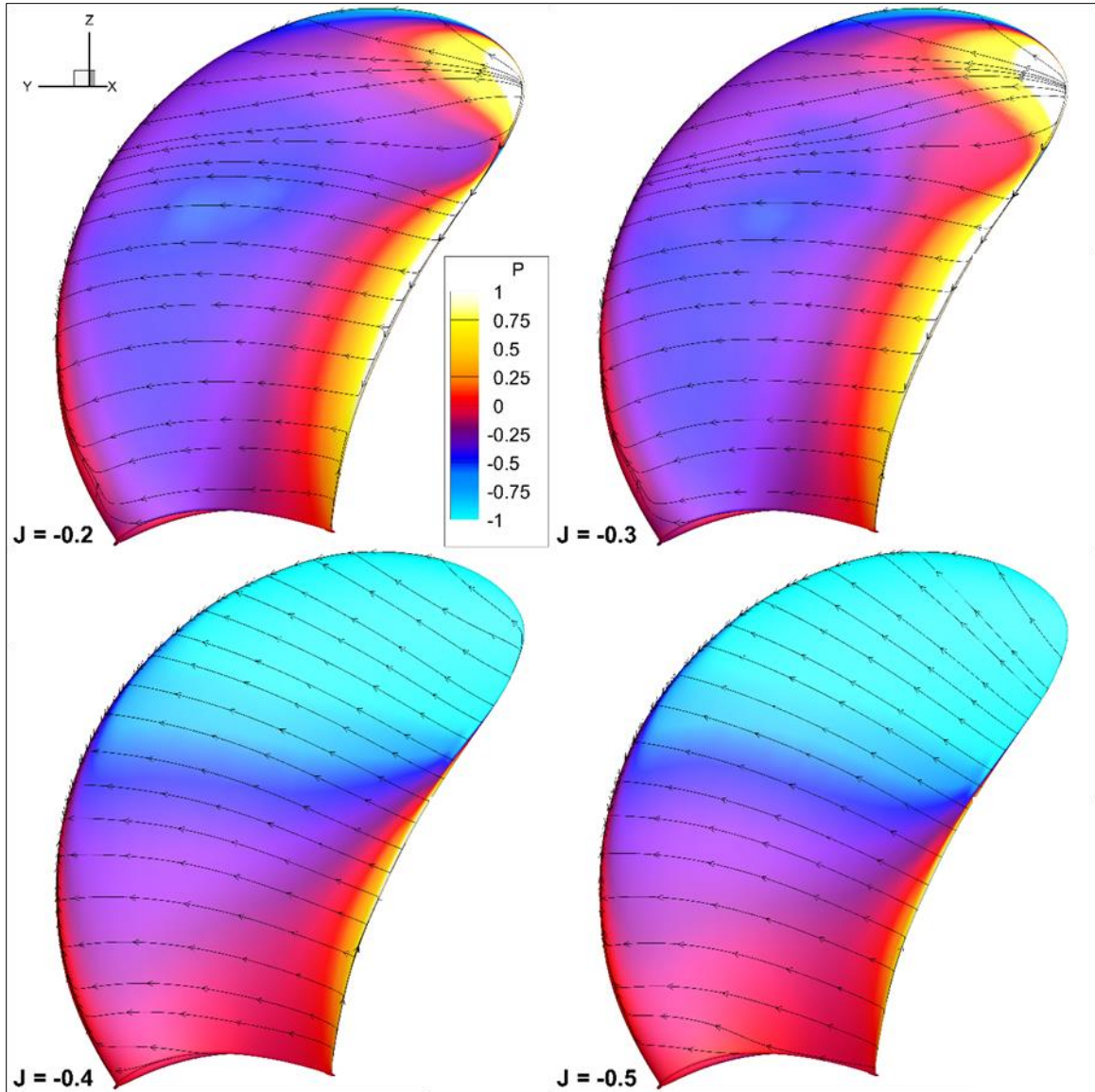
Figure 36: 7371R regime I and II blade pressure distribution on pressure side with streamlines. Phase average taken every rotation for 100 rotations. Streamlines are shown on grid points near the surface of the blade. Pressure contour non-dimensionalized by ρU_0^2.

Regime II cases show high levels of attached flow at all radial locations on both the pressure

and suction side of the propeller blades. Regime I streamlines show large radial deflection

of the flow near the leading edge and blade tip on the suction side and both convergent and

divergent streamlines at radial locations near the blade tip on the pressure side.

52
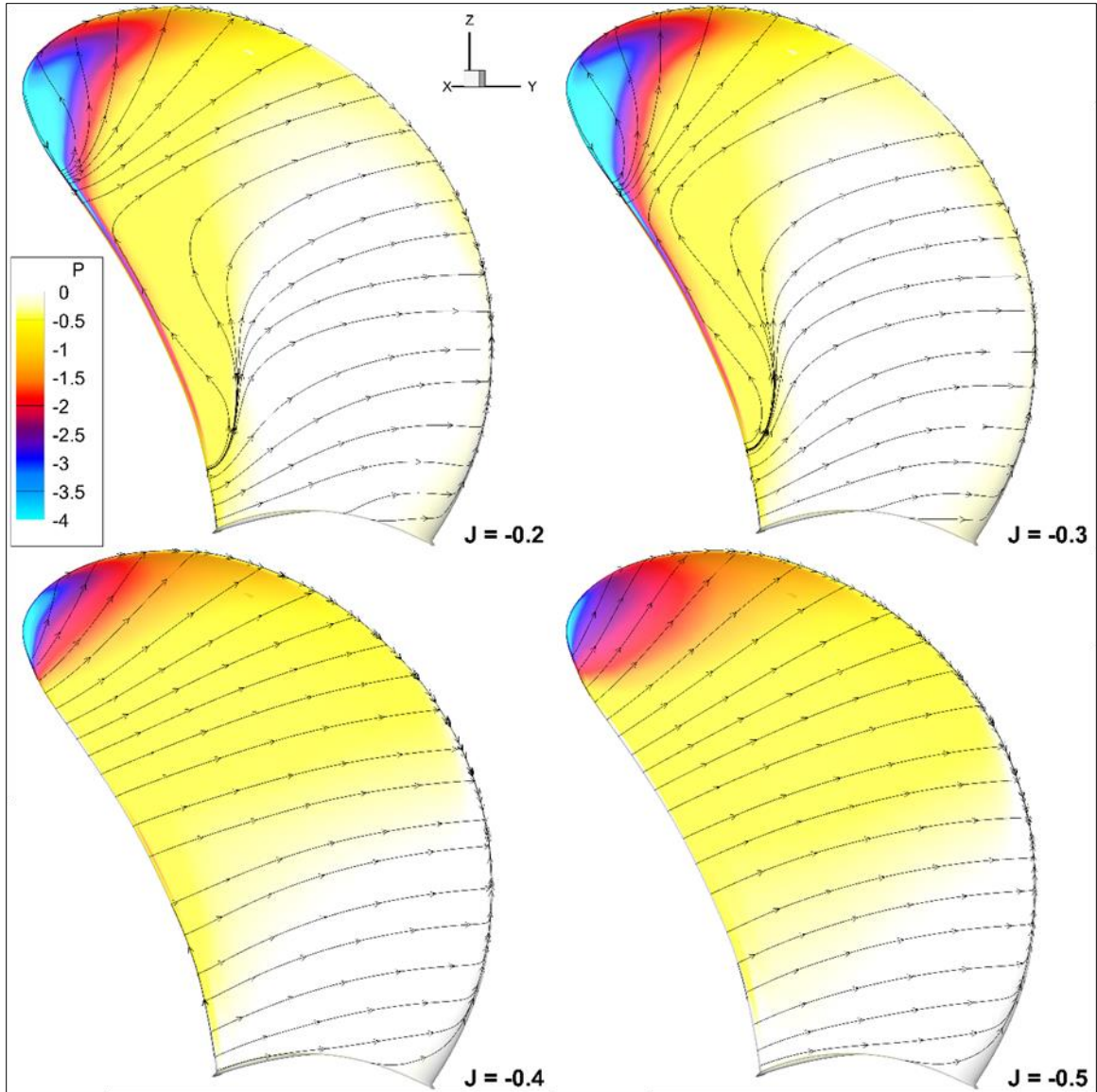
Figure 37: 7371R regime I and II blade pressure distribution on suction side with streamlines. Phase average taken every rotation for 100 rotations. Streamlines are shown on grid points near the surface of the blade. Pressure contour non-dimensionalized by ρU_0^2.

The difference in angle of attack and flow separations are shown by the 2D constant radius blade passage flow in Figure 38, with tangential velocity defined in the blade system. For regime II, the angle of the incoming velocity is consistently at small angles of attack at all radial locations along the span of the blade. This ensures that the flow stays highly attached and lower pressure gradients are created near the surface of the blade. The blade passage flow for regime I has a consistently favorable angle of attack to produce lower

53
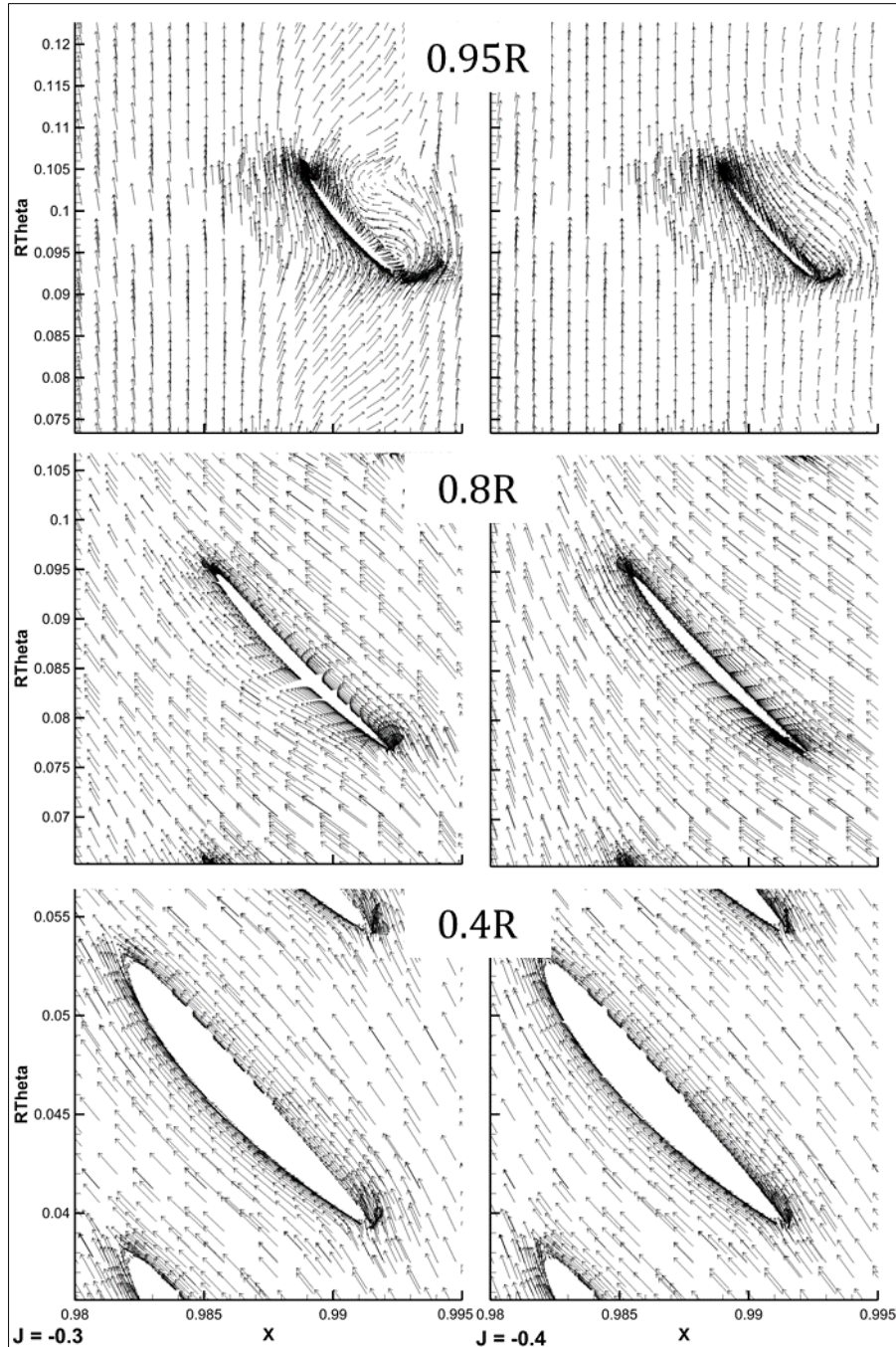
Figure 38: 7371R regime I and II constant radius 2D blade passage flows. J = -0.3 (left), -0.4 (right). Tangential velocity transformed into the blade system.

pressures on the suction side of the propeller. Near the tip for regime I, the incoming flow appears to come from the upstream side of the blade causing very large angles of attack and large flow separation on the suction side of the propeller. This flow is transported by the blade tip vortices that are tightly attached to the tips. The area of influence of the blade

tip vorticity can be seen on the left of Figure 38 at 0.95R, bounded by the vectors that have a small axial velocity component.

An alternative method for analyzing the difference of thrust is tracking the momentum transfer from the propeller output to the free-stream flow. Since the outflow of the propeller for regime I and II produces a closed recirculation, a direct fluid momentum transfer cannot be the main mechanism of thrust production. Instead, energy is transferred via turbulence produced by the propeller interacting with outer free-stream flow. Figure 39 contains the circumferential and temporal average of Reynolds stresses for J = -0.3 and -
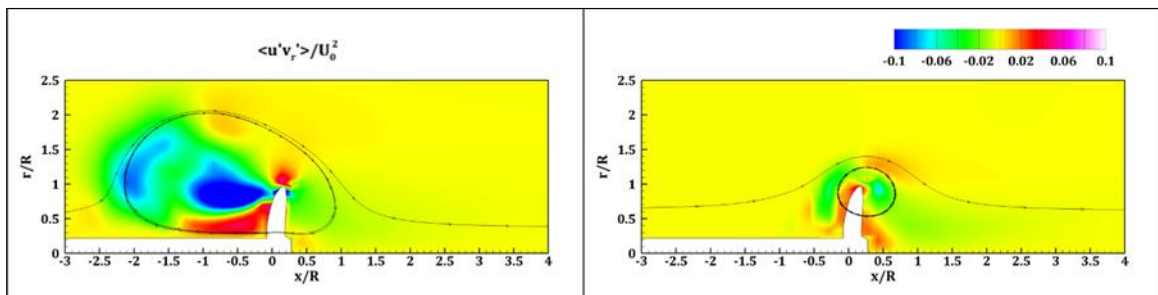
Figure 39: 7371R regime I and II temporal and circumferential averages of Reynolds stresses. J = -0.3 (top), J = -0.5 (bottom).

0.5. The closing streamline for the propeller recirculation is shown along with the bounding streamline that indicates the location of the free-stream. Large Reynolds stresses are produced by regime I upstream of the propeller where the jet of turbulent vorticity stagnates from blocking the free-stream flow. There is also an area of high Reynolds stress produced near the core of the jet where axial velocity is highest. For regime II, the area of influence of the circulation where the free-stream is diverted is much smaller than for regime I. The stable ring vortex circulation around the propeller tips does not produce high levels of turbulence as in regime II. This leads to overall lower Reynolds stresses produced by regime II.

55

4.4.2 Regime II→III, formation of wobbling asymmetric ring vortex and its effects on propeller forces

As was shown with the transition case of J = -1.0, regime III cases begin in regime II, forming an axisymmetric ring vortex before a portion of the ring vortex destabilizes and begins to stretch away from the propeller tips. Figure 40 contains the inflow and outflow discs of 7371R for regimes I, II and III. The left-hand side shows the axial velocity of the inflow disc and the right-hand side shows the change in axial velocity through the propeller on the outflow disc. In agreement with the phase average slice of J = -0.3 in Figure 12, the regime I case at the top of Figure 40 shows very little obstruction of the outflow with respect to the other regimes. Regime II (middle Figure 40) exhibits an obstruction along the outer radius of the propeller disc, while the inner radius shows lower flow blockage. As a portion of the regime II vortex builds in strength, this section remains attached to the blades and pushes the flow adjacent to it away from the propeller blades. This is shown on the right in Figure 40 for J = -0.6. The outflow for the portion of the ring vortex attached at the blade tips is obstructed, causing inflow on that side of the propeller disc to be diverted to the adjacent side of the propeller where the outflow is unobstructed. The circumferential positions at which the outflow is blocked closely bounds the position of the asymmetry of the ring vortex. This section of the ring vortex has a strong radial component, significantly breaking the axisymmetry of tangential and radial velocity exhibited by regimes I and II. This creates a high amplitude side-force seen in the horizontal side-force time histories of regime III cases in Figure 24. The asymmetric vortex state is very stable for 7371R, and rotates in the opposite direction of the propeller rotation (refer to Figure 23). As a result, the low frequency first harmonic is produced in the side-forces equal to the frequency of

56

rotation of the ring vortex. Additionally, the vertical and horizontal side-force time histories display similar behavior 90° out-of-phase of each other.
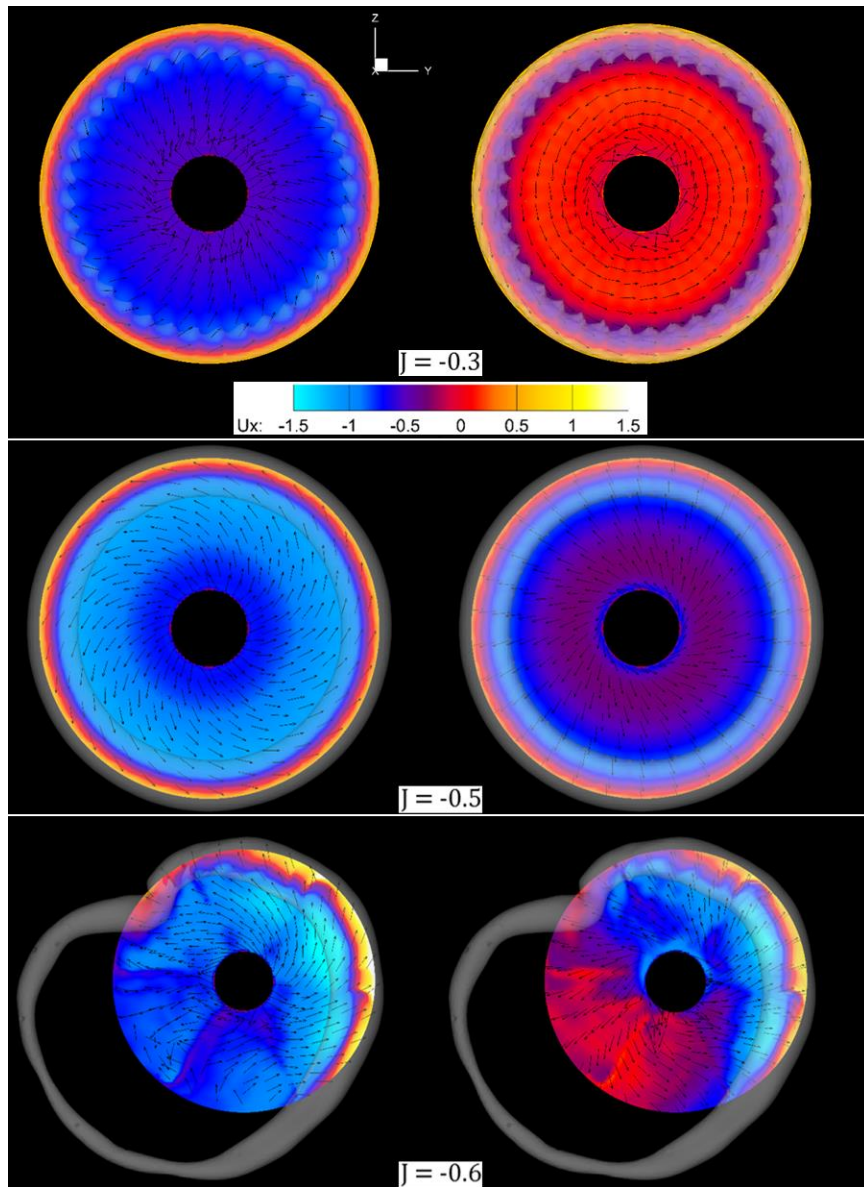
Figure 40: 7371R regime III development of ring vortex asymmetry. Inflow and outflow of regime I, II and III. Inflow propeller disk axial velocity (left) and change in axial velocity at outflow disc (right).Contour of axial velocity non-dimensionalized by nD. Uniform length vectors are in earth system. J = -0.3 and -0.5 are the 10° phase averages. J = -0.6 is a phase average of the ring vortex based on its position.

57

This obstructing of the outflow streamlines is introduced in Figures 41 and 42 below. Figure 41 is an instantaneous solution of J = -0.7 at rotation 55. The blades are numbered 1 through 6 counter-clockwise indicated in the figure. Figure 41. The background is a slice of axial velocity at the outlet of the propeller indicating the areas of blocked and unobstructed outflow. The outflow behind 1, 2 and 6 shows lower magnitude outflow velocity than the adjacent section where the ring vortex has been pushed away from the propeller disk. The blocking of outflow at blades 1, 2 and 6 is shown in Figure 42 as the tangentially deflected upstream vectors. This blockage rotates opposite to the propeller rotation direction giving the ring vortex its rotation.
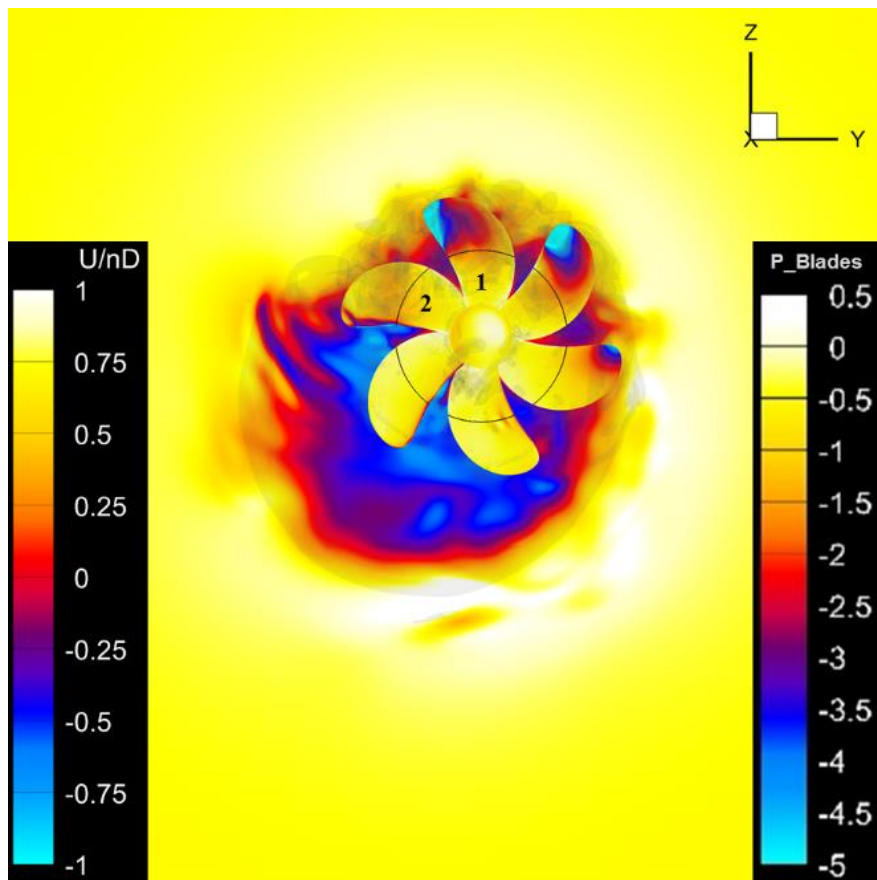
Figure 41: 7371R regime III outflow obstruction, J = -0.7. Ring Vortex resolved by iso-surface of Q-Criterion. Blades colored with pressure, non-dimensionalized by ρU_θ^2. Axial slice at propeller outlet colored with axial velocity nondimensionalized by nD. Radius location 0.6R shown by line on blades.

58
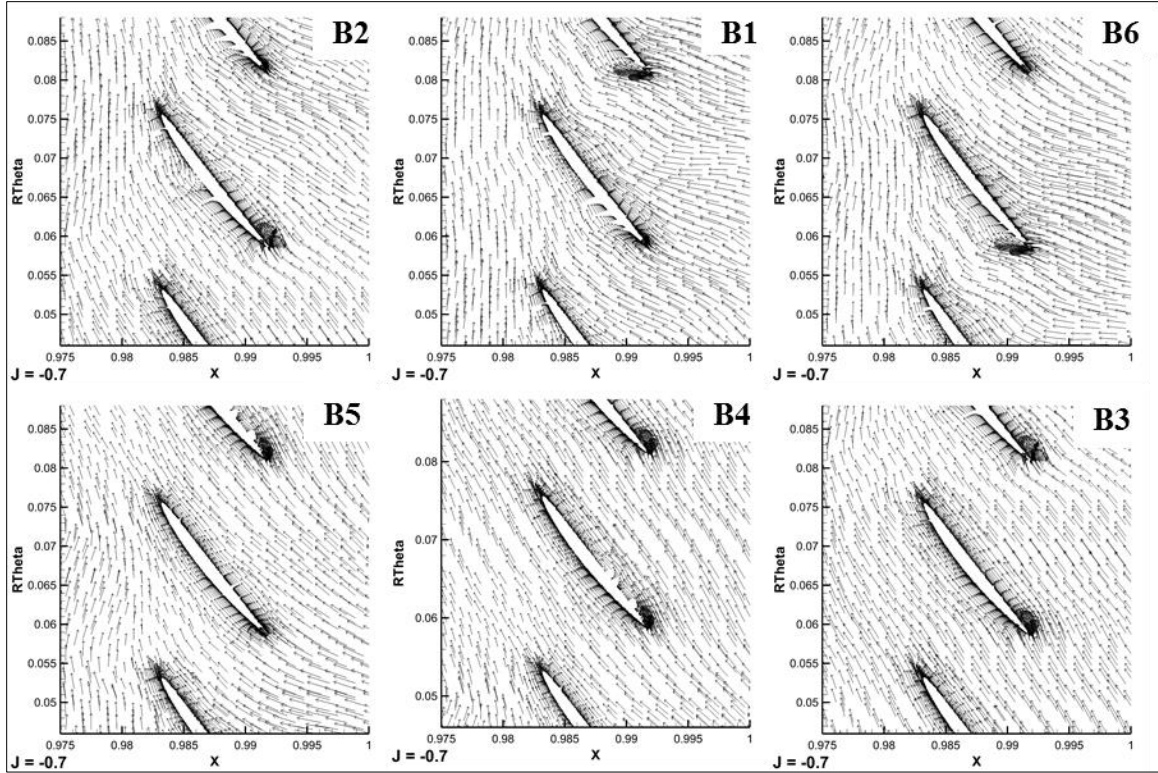
Figure 42: 7371R regime III constant radius 2D blade passage flows showing outflow obstruction, J = -0.7. Tangential velocity transformed into the blade system.

4.4.3 Regime III, wobbling expansion and contraction of ring vortex and its effects on thrust

Introduced by the PSDs of regime III cases for 7371R (Figure 25), a first harmonic begins to develop in thrust as advance coefficient magnitude increases. This first harmonic is not present for J = -0.6, begins to develop in J = -0.7 and is distinctly present for J = -0.8 and = -0.9. The source of the first harmonic is shown in Figure 43. At the top of Figure 43 is an instantaneous solution corresponding to a minimum in thrust, and at the bottom a maximum in thrust for J = -0.7, -0.8 and -0.9. The solution has been put into the ring vortex system such that it does not rotate around the propeller axis. This was done using a rotational phase shift of the first harmonic frequency found for the side-forces. When thrust is minimum, the stretched section of the ring vortex contracts towards the blade tips, resulting in a more constricted flow, as in regime II, reducing the strength of the ring vortex.

59
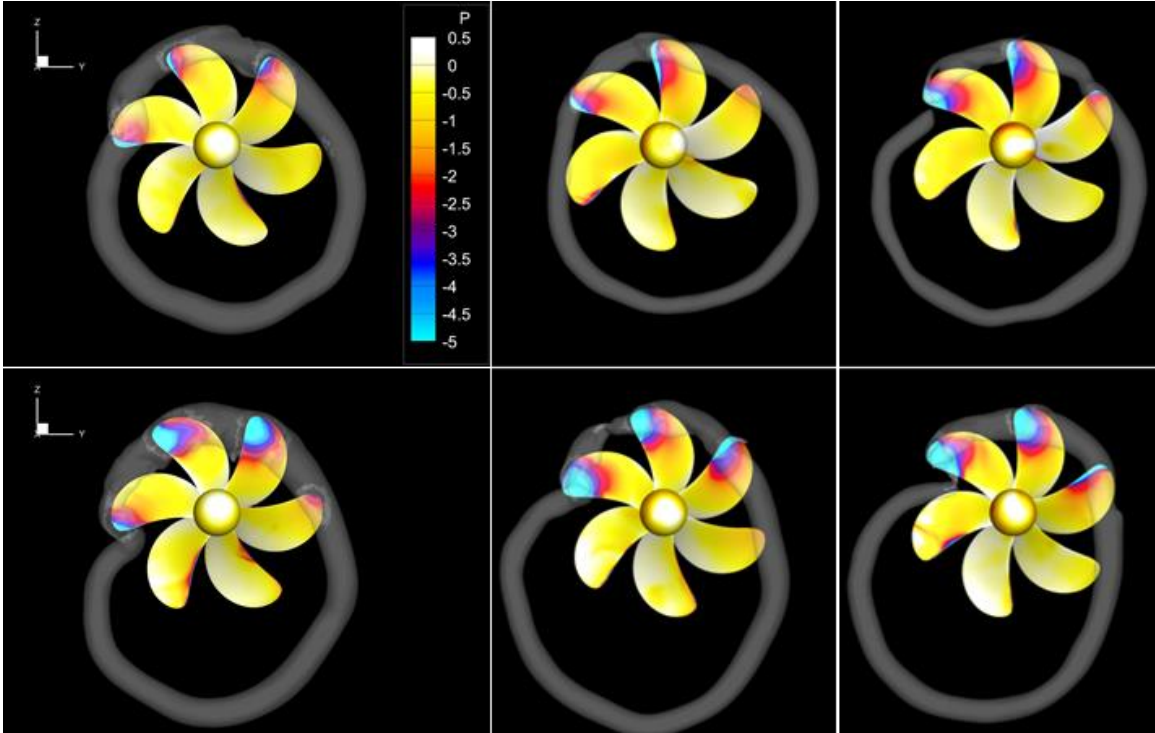
Figure 43: 7371R regime III first harmonic of thrust. Instances of max thrust and minimum thrust.Min thrust (top), max thrust (bottom) for J = -0.7, -0.8, -0.9 (left to right). Ring vortex is resolved by isosurface of pressure, blade pressure distributions shown on suction side, non-dimensionalized by ρU_0^2.

At a maximum of thrust, the stretched section of the ring vortex expands away from the propeller blades and the section of the ring vortex attached to the propeller blades. The flow through the stretched section of the ring vortex becomes less constricted, allowing the ring vortex to grow in strength.

When the thrust is at a maximum, the stronger ring vortex creates more favorable blade pressure. Figure 44 contains the blade pressure contours on the pressure and suction side at a maximum state of propeller thrust (left) and a minimum state of propeller thrust (right). Both sides of Figure 44 are at a state of maximum thrust at the blade level for blade 1, indicated by the square cursor at the bottom of the figure. The time history of the blade

60

forces illustrate the source of the increase in propeller thrust at the blade force level. Specifically, an additional large spike is present at maximum blade thrust when propeller thrust is maximum. Referring to the position indicator at the corner of the pressure figures,
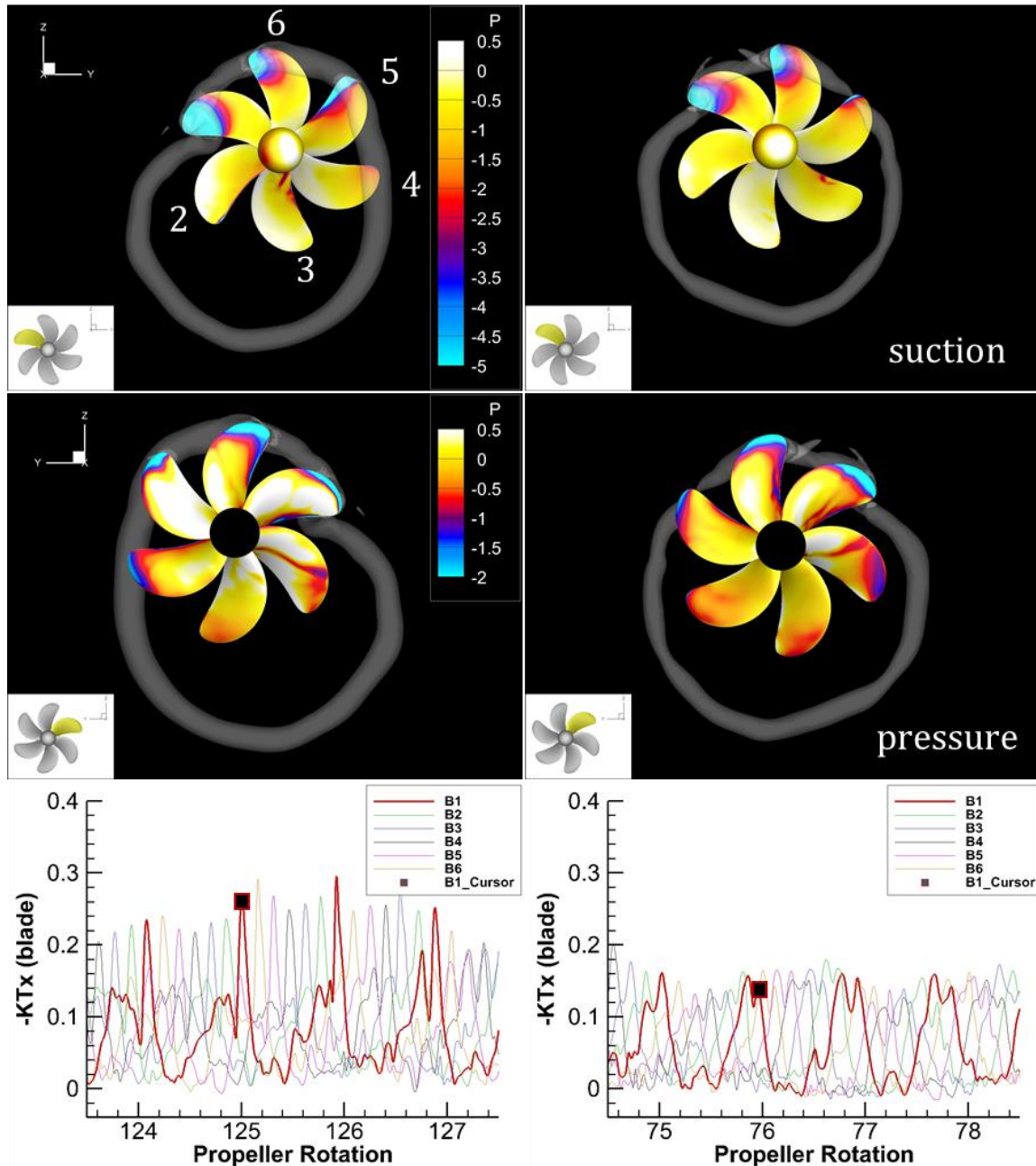
Figure 44: 7371R regime III first harmonic of thrust. Blade force contributions to min and max thrust.Max (left) and min thrust (right) for first harmonic of thrust, J = -0.9. Blade pressure contours are shown for the suction side (top) and pressure side (middle), non-dimensionalized by ρU_θ^2. Blade thrust time histories (bottom) with the time instance of blade 1 indicated by the black cursor. The position of blade 1 is indicated by the image in the bottom left corner of each instantaneous flow solution. Ring vortex is resolved by isosurface of pressure.

61

this corresponds to the point at which the blade is interacting with the kinked attachment point. Large blade tip loading occurs during this interaction displayed on the suction side contours. This loading is much higher when the ring vortex is expanded and propeller force is maximum. Other contributions to increased thrust are indicated in Figure 44. Due to the increased strength of the ring vortex, blade 5 has higher leading edge loading when propeller thrust is maximum. In general, larger positive pressures are produces on the pressure side of the blades for maximum propeller thrust state.

4.4.4 Regime IV, massive flow separation and blade passage penetration

Once free-stream flow reaches a critical value, incursion by the incoming upstream flow into the propeller disc occurs along the bottom half of the blades. This destroys the upstream to downstream circulation that produces a ring vortex. Figure 45 shows the blade pressure distributions with streamlines showing the flow near the surface. Large positive pressure is shown on the pressure side, due to blade passage penetration by the free-stream flow. Streamlines near the root diverge tangentially toward the leading and trailing edges on the pressure side, showing the areas of strongest blade passage penetration. The flow toward the tip of the blades has a large radial component on both the pressure and suction side, indicating the diverted free-stream flow on the pressure side by the blades and the circulating wake behind the propeller. Constant radial plots on the left of Figure 45 show the blade passage penetration near the roots which is the largest contributor to side-force magnitude. The combination of the high pressure on the pressure side and the large suction from flow separation on the leading edge of the pressure side combine to produce the large thrust values.
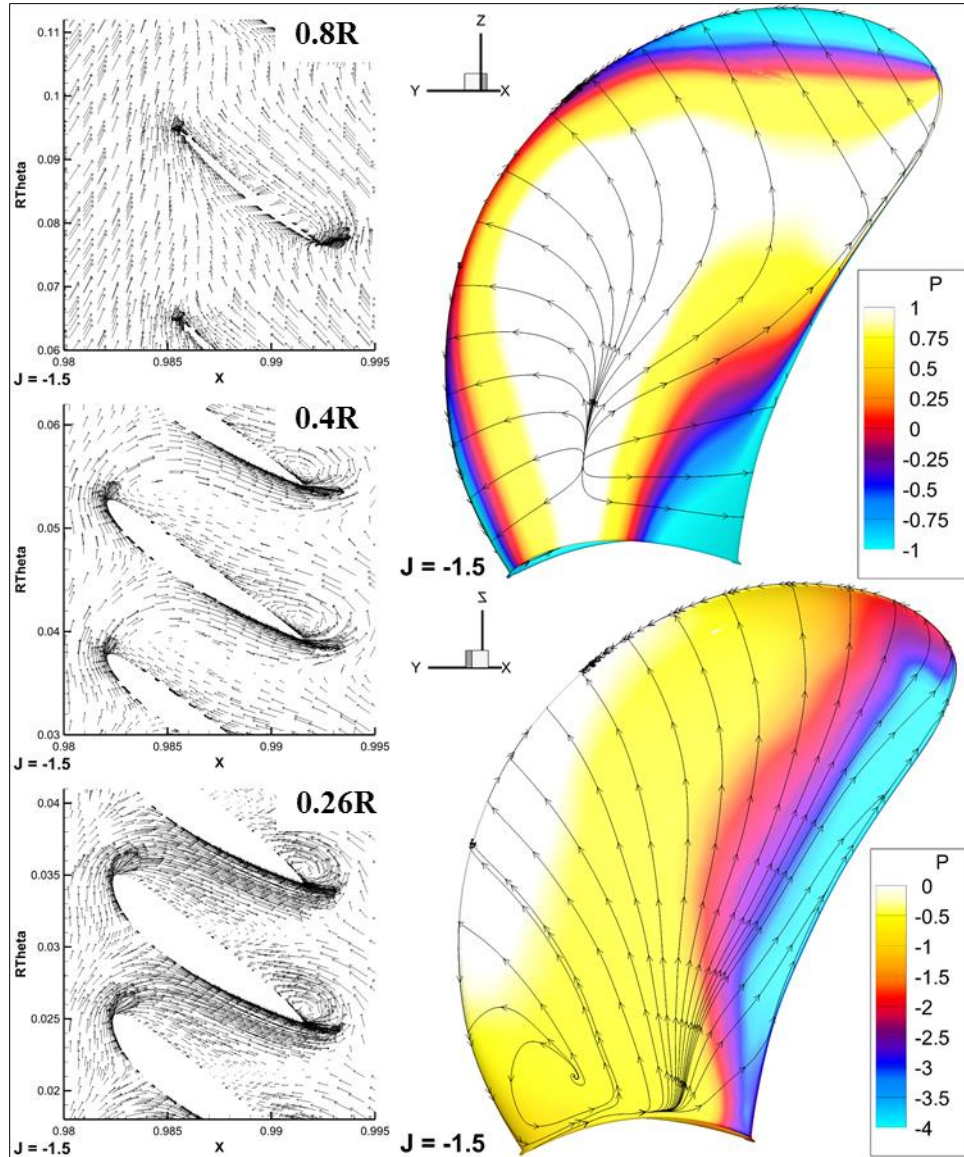
62

Figure 45: 7371R regime III constant radius 2D blade passage flows and blade pressure distribution on suction side and pressure side with streamlines. Blade pressure distributions (pressure side top, suction side bottom) are shown with streamlines on points near the blade surface (right), non-dimensionalized by ρU₀². Constant radius R-θ plots with tangential vectors (left).

4.5 Application to Joubert BB2 Submarine with 7371R Propeller in Crashback

No experimental data is available for steady-state crashback operation for 7371R. However, experimental crashback data for a free-running Joubert BB2 model with a stock 7371R propeller equipped is available (Overpelt, 2015). Details on REX simulations and comparison with experimental data are presented in Carrica et al. (2016). A 20 degree max q surfacing maneuver was concluded with a crashback maneuver in order to stop the free-running
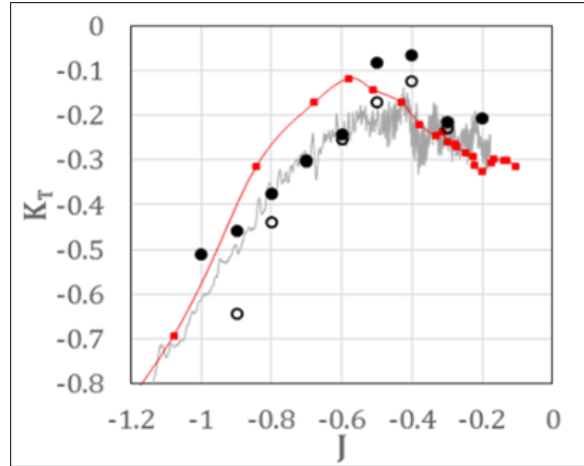
Figure 46: 7371R in computational and experimental free-running crashback maneuver, comparison with steady-state crashback OWC. Joubert BB2 experiment by Overpelt (2015) (red line), Joubert BB2 REX results from Carrica et al. (2016) (grey line), REX steady-state DDES for 0° (solid symbols) and 10° (open symbols) shaft angle. Experimental data is shown in 1.07s intervals (red symbols).

model. The time history of the experimental stopping maneuver plotted in the third quadrant of the OWC is compared to an equivalent free-running simulation performed using REX and DDES REX steady-state crashback results for 0° and 10° shaft angle in Figure 46. The crashback maneuver was performed at the end of a surfacing test by rapidly reversing the direction of propeller rotation after the bow breached the free surface and re-entered the water. This caused the submarine to start at a large magnitude advance coefficient and decrease to a smaller magnitude advance coefficient throughout the stopping maneuver. Uniform propeller rotational speed was not achieved until J = -0.4. Additionally, the pitch and yaw of the submarine varied between from -5° to 15° and from 0° to -10°, respectively and the distance of the free-running submarine from the free-surface differed between experiment and simulation. These differences are shown in Figure 47.

64

Despite the varying of propeller rotational speed for the free-running submarine and the varying incoming flow angle, CFD and experimental results for the submarine maneuver show good agreement with steady-state DDES results, which had constant rotational speed and incoming flow angle.
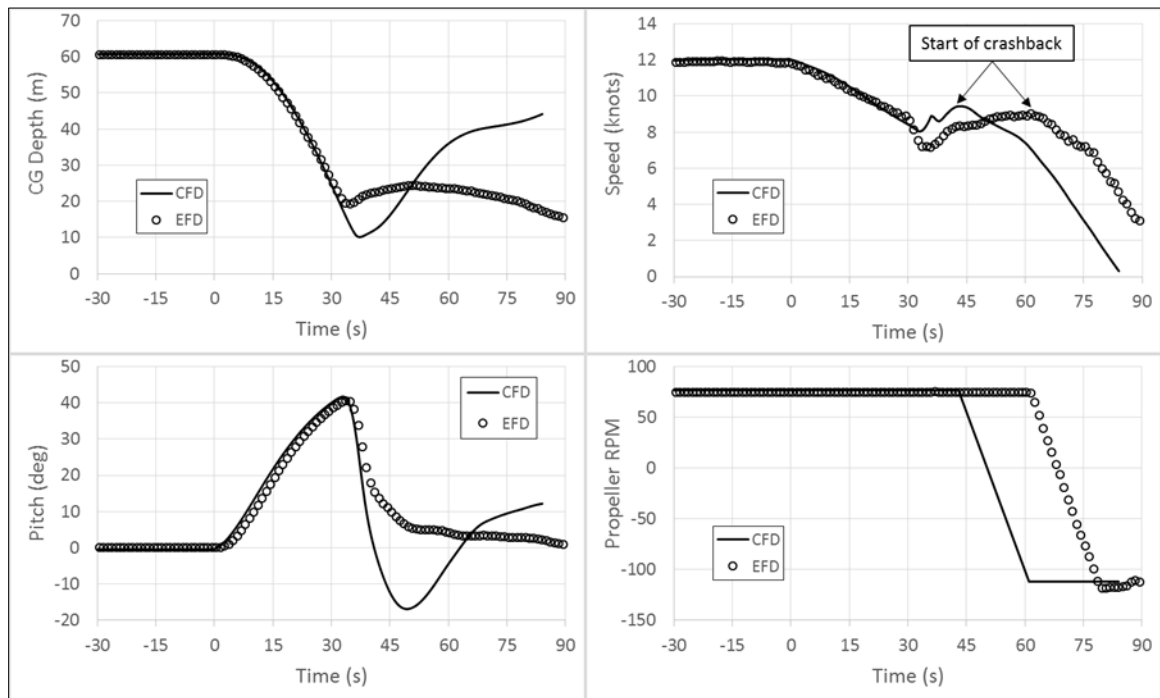
Figure 47: 7371R free-running submarine maneuver details. Comparison between experiment and simulation for free-running 20 degree max q surface maneuver. DSTO/MARIN Joubert BB2 model equipped with MARIN 7371R propeller. Experimental data from Overpelt (2015) and CFD data from (Carrica et al., 2016).

Figure 48 shows an instantaneous flow solution of the maneuver at a time point where the advance coefficient was approximately J = -1.0. This operational point was shown to exhibit flow behavior of regime II, III and IV in a previous section for steady-state open-water simulations. For the time point shown, regime III behavior of an asymmetric, tilted ring vortex is captured. The resolved ring vortex includes important unique features mentioned in the description of regime III in previous sections. These include attachment on 4 blades, detachment from the remaining adjacent blades and a kink

65

on one end of the attached section of the ring vortex. A large tilt to the ring vortex is shown, which occurred in steady-state simulations of J = -1.0 before the ring vortex detached.

Figure 48: 7371R free-running submarine maneuver instantaneous flow field showing ring vortex. Joubert BB2 equipped with 7371R propeller.The advance coefficient pictured is approximately J = -1.0. Ring vortex is resolved by three iso-surfaces of pressure of varying transparency.

Chapter 5: Conclusions and Future Work

5.1 Conclusions

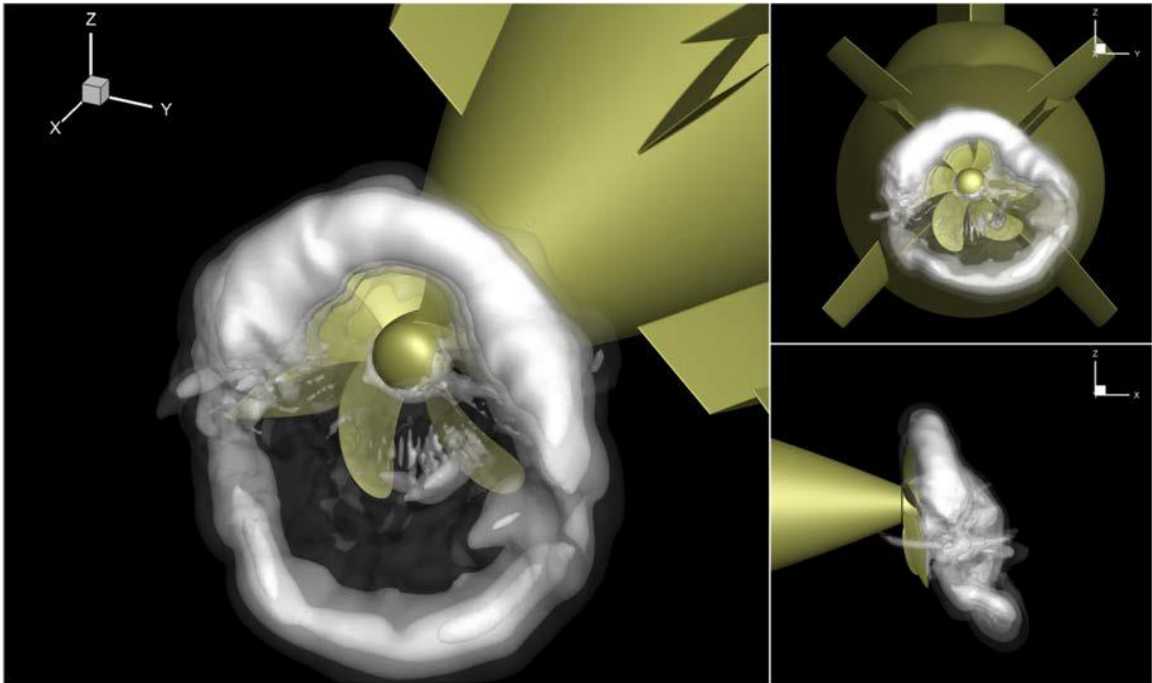A simulation study of crashback was performed for two propellers. DDES computations of DTMB 4381 and MARIN 7371R were validated in ahead condition, and only DTMB 4381 was compared with data in crashback condition. Both propellers agreed well with experimental data in ahead condition. For crashback, thrust and torque coefficients for simulations fell between lower magnitude water tunnel and higher magnitude open-water experimental results. Previous studies have broadly attributed differences between water tunnel and open-water 4381 experiment force results to wall proximity, tunnel shear layer, and shaft location effects. Given the mixed agreement that the open-water simulation results had with water tunnel or open-water domains, the proposed influences are likely specific to the advance coefficient. Tunnel blockage effects are more plausible at low magnitude advance coefficients, where an upstream traveling jet produced by the propeller interacts with the inlet flow. At moderate advance coefficients near the minimum thrust and torque point, the small area of influence of the recirculation near the propeller disk is less perturbed by distant boundary effects, and only the shaft causes disturbances in the small recirculation zone. An asymmetric ring vortex is predicted by the simulations at higher advance coefficients. The vortex influences the flow radially adjacent to the propeller disk, to a greater extent than for flow regimes where symmetric ring vortices are observed. Consequently, the water tunnel nozzle shear layer and the proximity of the LES lateral boundaries could influence the temporal consistency of ring vortex behavior. If these effects weaken the ring vortex, forcing it into a tighter configuration near the blade tips, the time average of the side-forces would be significantly

67

influenced. This influence would have a larger effect on side-forces compared to thrust due to side-forces extreme dependence on the asymmetry severity of the radial flow.

Propeller 7371R crashback results exhibited four distinct and remarkably stable flow regimes. The range of advance coefficients at which each type of flow behavior is produced is wider for 7371R than it is for 4381. Regime II flow behavior was not observed in simulations of 4381, implying an extremely narrow operating range for stable regime II behavior to exist in. Overall, each flow regime behavior appeared more stable for 7371R than 4381. Regime I was identified as an upstream jet of turbulent structures, forming two areas of circulation. Regime II is a strongly axisymmetric ring vortex attached behind the propeller near the blade tips. From regime I to regime II, a large drop in thrust was attributed to an overall decrease in angle of attack and a decrease in energy transferred to the free-stream by means of turbulent structures. Formation of the asymmetric ring vortex of regime III was attributed to instability in the vortex of regime II. A section of the ring vortex grows in strength pushing the adjacent section of the ring vortex away from the propeller disc as a consequence of the stronger radial component of its induced inflow. The distancing of the ring vortex from the blade tips weakens the vortex, allowing axial flow to move freely through the propeller plane and upstream against the incoming free-stream flow. The stretched section of the ring vortex creates asymmetry in the radial flow. This asymmetric ring vortex rotates around the propeller axis opposite the propeller's rotational direction at a frequency much lower than propeller rotational frequency. This produces strong harmonics in the horizontal and vertical side-forces. A higher order instability was observed for regime III as advance coefficient increased in magnitude. This higher order instability took the form of an expansion and contraction of the asymmetric ring vortex. As

68

a result of this deformation of the asymmetric ring vortex, a low-frequency harmonic developed in propeller thrust. Maximum thrust occurs when the ring vortex expands, minimum thrust when the ring vortex contracts. A grid study showed good convergence of thrust and resultant side-force values between three levels of refinement. Flow behavior was predominately consistent between grids. However, a first harmonic in thrust appeared to become more defined with increasing grid resolution. As free-stream momentum increases, it dominates the output of the propeller causing free-stream penetration of the blade passages, leading to regime IV. In this regime, a large circulating wake structure forms behind the propeller, with no distinct vortex structure able to form. This transition is believed to occur at $J \cong -1.0$ for 7371R.

69

5.2 Suggested Future Work

The temporal randomness of the flow behavior introduces significant statistical uncertainty into the analysis. All cases were run for at least 150 rotations, which was enough to perform the initial analysis. To improve statistical certainty and confidence in observed flow behavior more simulation time is required for all cases. More simulations near the transition from regime I to II for 7371R are required to determine whether there is a multi-modal flow behavior similar to those observed for J = -1.0. Additionally, a grid study should be performed at advance coefficients near a transition to another regime for 7371R to evaluate effects of grid resolution on regime transition. To identify more features of the regimes, a modal analysis could be performed. This could extract higher order modes that cannot be determined easily using the methods mentioned. Oblique flow angles could be studied to determine the effects of a breakdown of incoming flow symmetry with respect to propeller rotation. As an extension to the open-water steady-state simulations of 7371R in crashback, simulations with a submarine hull included could be performed to study changes in flow regime behavior of 7371R. This could include steady-state simulations with no hull motions and no appendages or appendages added (i.e. sternplanes, etc.). Transient simulations of crashback self-propulsion with no hull motions to study transient effects and relate to steady-state transition operation points such as J = -1.0. Steady-state and transient simulations allowing the submarine to pitch and/or yaw to determine flow angle effects on side-forces and thrust.

70

References

Carrica, P. M., Wilson, R. V., Noack, R. W., & Stern, F. (2007a). Ship motions using single-phase level set with dynamic overset grids. *Computers & fluids*, *36*(9), 1415-1433.

Carrica, P. M., Wilson, R. V., & Stern, F. (2007b). An unsteady single-phase level set method for viscous free surface flows. *International Journal for Numerical Methods in Fluids*, *53*(2), 229-256.

Carrica, P. M., Paik, K. J., Hosseini, H. S., & Stern, F. (2008). URANS analysis of a broaching event in irregular quartering seas. *Journal of Marine Science and Technology*, *13*(4), 395-407.

Carrica, P.M., Kerkvliet, M., Quadvlieg, F., Pontarelli, M., Martin, J.E. (2016). CFD Simulations and Experiments of a Maneuvering Generic Submarine and Prognosis for Simulation of Near Surface Operation. In *Proceedings of 30th Symposium on Naval Hydrodynamics, Hobart, Australia.*

Chang, P. A., Ebert, M., Young, Y. L., Liu, Z., Mahesh, K., Jang, H., & Shearer, M. (2008). Propeller forces and structural response due to crashback. In *27th Symposium on Naval Hydrodynamics*.

Chen, B., & Stern, F. (1999). Computational fluid dynamics of four-quadrant marine-propulsor flow. *Journal of Ship Research*, *43*(4), 218-228.

Ebert, M., Chang, P. A. & Mulvihill, L. (2007). NSWCCD FY07 crashback computational effort. *In ONR Propulsor S & T Program Review*

Esmaeilpour, M., Martin, J. E., & Carrica, P. M. (2016). Near-field flow of submarines and ships advancing in a stable stratified fluid. *Ocean Engineering*, *123*, 75-95.

Green, R. B., Gillies, E. A., & Brown, R. E. (2005). The flow field around a rotor in axial descent. *Journal of Fluid Mechanics*, *534*, 237-261.

Hecker, R., & Remmers, K. (1971). Four Quadrant Open-Water Performance of Propellers 3710, 4024, 4086, 4381, 4382, 4383, 4384 and 4426. *David Taylor Naval Ship Research and Development Center, report NSRADC*, 417-H01.

Hough, G. R., & Ordway, D. E. (1965). The Generalized Actuator Disk, Developments in Theoretical and Applied Mechanics, Vol. II.

Jang, H., & Mahesh, K. (2013). Large eddy simulation of flow around a reverse rotating propeller. Journal of Fluid Mechanics, 729, 151-179.

Jiang, C. W., Dong, R. R., Liu, H. L., & Chang, M. S. (1997). 24-inch water tunnel flow field measurements during propeller crashback. In *21st Symposium on Naval Hydrodynamics, The National Academies Press, Washington, DC* (pp. 136-146).

Jessup, S., Fry, D., & Donnelly, M. (2006) Unsteady propeller performance in crashback conditions with and without a duct. In *Proceedings of the 26th Symposium on Naval Hydrodynamics, Rome, Italy*.

Jessup, S., Chesnakas, C., Fry, D., Donnelly, M., Black, S., & Park, J. (2004). Propeller performance at extreme off design conditions. In *Proceedings of the 25th Symposium on Naval Hydrodynamics, St. John's, Canada*.

Johnson, W. (2005). Model for vortex ring state influence on rotorcraft flight dynamics.

Kerwin, J. E., Kinnas, S. A., Lee, J. T., & Shih, W. Z. (1987). *A surface panel method for the hydrodynamic analysis of ducted propellers*. MASSACHUSETTS INST OF TECH CAMBRIDGE DEPT OF OCEAN ENGINEERING.

Li, J., Castro, A. M., & Carrica, P. M. (2015). A pressure–velocity coupling approach for high void fraction free surface bubbly flows in overset curvilinear grids. *International Journal for Numerical Methods in Fluids*, *79*(7), 343-369.

Li, Y., Castro, A. M., Sinokrot, T., Prescott, W., & Carrica, P. M. (2015). Coupled multi-body dynamics and CFD for wind turbine simulation including explicit wind turbulence. *Renewable Energy*, *76*, 338-361.

Mahmoudi, M., & Fleck, B. A. (2016). Experimental Measurement of the Velocity Field of Round Wall Jet in Counterflow. *Journal of Hydraulic Engineering*, *143*(1), 04016076.

Martin, J. E., Mofidi, A., Michael, T., & Carrica, P. M. (2015). Validation of a propeller model for maneuvering applications. In *Proceedings of 4th International Symposium on Marine Propulsors*, Austin, Texas, USA

Menter, F. R. (1994). Two-equation eddy-viscosity turbulence models for engineering applications. *AIAA journal*, *32*(8), 1598-1605.

Noack, R. W., & Boger, D. A. (2009). Improvements to suggar and dirtlib for overset store separation simulations. *Proceedings of the 47th AIAA Aerospace Science and Exhibit*.

Overpelt, B. (2015). Free-running manoeuvring model tests on a modern generic SSK class submarine (BB2), In *Proceedings of PACIFIC 2015 Int. Maritime Conf., Sydney, NSW, Australia*

Pontarelli, M., Martin, J. E., Carrica, P. M. (2017). Dynamic Instabilities in Propeller Crashback. In *Proceedings of 5th International Symposium on Marine Propulsors*, Espoo, Finland

Paik, K. J., Carrica, P. M., Lee, D., & Maki, K. (2009). Strongly coupled fluid–structure interaction method for structural loads on surface ships. *Ocean Engineering*, *36*(17), 1346-1357.

Vyšohlíd, M., & Mahesh, K. (2006). Large eddy simulation of crashback in marine propellers. In *Proceedings of the 26th Symposium on Naval Hydrodynamics, Rome, Italy* (Vol. 9, pp. 237-261). Office of Naval Research.

Xing, T., Carrica, P., & Stern, F. (2010). Large-scale RANS and DDES computations of KVLCC2 at drift angle 0 degree. *Proceedings of Gothenburg*.

Xing, T., Shao, J., & Stern, F. (2007). BKW-RS-DES of unsteady vortical flow for KVLCC2 at large drift angles. In *Proceedings of the 9th International Conference on Numerical Ship Hydrodynamics, Ann Arbor, Michigan, Aug* (pp. 5-8).

Yang, J., Sakamoto, N., Wang, Z., Carrica, P., & Stern, F. (2007, August). Two phase level-set/immersed-boundary Cartesian grid method for ship hydrodynamics. *In Proc. Ninth Int. Conf. Numer. Ship Hydrodynamics*, Ann Arbor, MI (Vol. 24).

Zierke, W. C., Boger, D. A., Davoudzadeh, F., & McDonald, H. (1997). *A physics-based means of computing the flow around a maneuvering underwater vehicle* (No. ARL/PSU-TR-97-002). PENNSYLVANIA STATE UNIV STATE COLLEGE APPLIED RESEARCH LAB.